



# Electric field stimulates production of highly conductive microbial OmcZ nanowires

Sibel Ebru Yalcin<sup>1,2,7</sup> ✉, J. Patrick O'Brien<sup>1,2,7</sup>, Yangqi Gu<sup>2,3</sup>, Krystle Reiss<sup>4</sup>, Sophia M. Yi<sup>1,2</sup>, Ruchi Jain<sup>1,2</sup>, Vishok Srikanth<sup>1,2</sup>, Peter J. Dahl<sup>1,2</sup>, Winston Huynh<sup>2,5</sup>, Dennis Vu<sup>1,2</sup>, Atanu Acharya<sup>1,4</sup>, Subhrajyoti Chaudhuri<sup>4</sup>, Tamas Varga<sup>1,6</sup>, Victor S. Batista<sup>4</sup> and Nikhil S. Malvankar<sup>1,2</sup> ✉

**Multifunctional living materials are attractive due to their powerful ability to self-repair and replicate. However, most natural materials lack electronic functionality. Here we show that an electric field, applied to electricity-producing *Geobacter sulfurreducens* biofilms, stimulates production of cytochrome OmcZ nanowires with 1,000-fold higher conductivity (30 S cm<sup>-1</sup>) and threefold higher stiffness (1.5 GPa) than the cytochrome OmcS nanowires that are important in natural environments. Using chemical imaging-based multimodal nanospectroscopy, we correlate protein structure with function and observe pH-induced conformational switching to  $\beta$ -sheets in individual nanowires, which increases their stiffness and conductivity by 100-fold due to enhanced  $\pi$ -stacking of heme groups; this was further confirmed by computational modeling and bulk spectroscopic studies. These nanowires can transduce mechanical and chemical stimuli into electrical signals to perform sensing, synthesis and energy production. These findings of biologically produced, highly conductive protein nanowires may help to guide the development of seamless, bidirectional interfaces between biological and electronic systems.**

All commercial bioelectronic devices so far rely on the same silicon-based electronics that sustain global information technology and infrastructure<sup>1</sup>. Despite decades of effort, however, most synthetic and molecular electronic materials remain bio-incompatible and nonbiodegradable, and they usually show poor performance due to structural disorder<sup>1</sup>. Capital costs of equipment for their top-down manufacturing are also rising to \$14B per semiconductor fabrication plant<sup>2</sup>. In contrast, biological systems can construct nanomaterials at low cost and high yield from the bottom up<sup>2</sup>. Nonredox proteins have been shown to be conductive in single-molecule measurements, with small electron decay with distance, provided that charge is injected into the protein interior via good contact<sup>3</sup>. However, the conduction mechanism is unknown.

The common soil bacterium *G. sulfurreducens* naturally produces conductive protein filaments called ‘microbial nanowires’ to export electrons to extracellular electron acceptors, allowing the bacteria to respire in harsh environments that lack soluble, membrane-permeable, electron acceptors such as oxygen<sup>4</sup>. These nanowires have been thought to be type 4 pili, composed of PilA protein<sup>5</sup>. However, structural analysis found nanowires made up of cytochrome OmcS, with seamless stacking of hemes providing a continuous path for electrons (Extended Data Fig. 1a)<sup>4</sup>. OmcS is essential for bacterial electron transfer to Fe(III) oxide, one of the most abundant minerals in natural soil and sediment environments<sup>6</sup>. In addition to this short-range (~1–2  $\mu$ m) electron transfer to minerals via OmcS, *G. sulfurreducens* generates high current density by forming 100- $\mu$ m-thick conductive biofilms on electrodes under the influence of electric field in bioelectrochemical systems, even in the absence of OmcS<sup>7</sup>. Previous studies found that another cytochrome

OmcZ is not involved in electron transfer to Fe(III) oxide<sup>8</sup>, but it is essential for these biofilms generating high current density in bioelectrochemical systems<sup>9</sup>. However, immunogold labeling did not show OmcZ throughout these biofilms, but rather accumulation of OmcZ near the electrode surface<sup>10</sup>. As cytochromes were considered monomeric<sup>4</sup>, previous studies<sup>9–11</sup> presumed that cells may use isolated OmcZ monomers for short-range electron transfer at the biofilm–electrode interface. Therefore, the mechanism for long-range (~100  $\mu$ m) electron transport in current-producing biofilms has remained unknown.

To determine the composition, structure, electrical and mechanical properties of individual nanowires that confer conductivity to current-producing biofilms, we combined four complementary nanoscopic tools in a multimodal imaging platform (Extended Data Fig. 1a): (1) high-resolution atomic force microscopy (AFM) to identify the protein composition and morphology; (2) infrared (IR) nanospectroscopy using scattering-type scanning near-field optical microscopy (s-SNOM)<sup>12</sup> to identify biomolecules through their characteristic IR vibrational signatures; (3) conducting-probe-AFM (CP-AFM) to measure electron transport along the nanowire length and (4) nanomechanical AFM to determine nanowire stiffness. To further investigate the structural features in nanowires that enhance conductivity, we complemented these nanoscale studies with protein modeling and molecular dynamics simulations, cryo-electron microscopy (cryo-EM), as well as bulk measurements using X-ray diffraction (XRD), Fourier-transform IR spectroscopy (FTIR), circular dichroism (CD), Raman and fluorescence spectroscopy.

Using this suite of complementary imaging and spectroscopy methods, here we demonstrate that growing *G. sulfurreducens* biofilms in an electric field stimulates production of previously unknown

<sup>1</sup>Department of Molecular Biophysics and Biochemistry, Yale University, New Haven, CT, USA. <sup>2</sup>Microbial Sciences Institute, Yale University, New Haven, CT, USA. <sup>3</sup>Department of Molecular, Cellular & Developmental Biology, Yale University, New Haven, CT, USA. <sup>4</sup>Department of Chemistry, Yale University, New Haven, CT, USA. <sup>5</sup>Department of Biomedical Engineering, Yale University, New Haven, CT, USA. <sup>6</sup>Environmental Molecular Sciences Laboratory, Pacific Northwest National Laboratory, Richland, WA, USA. <sup>7</sup>These authors contributed equally: Sibel Ebru Yalcin, J. Patrick O'Brien.

✉e-mail: [sibel.yalcin@yale.edu](mailto:sibel.yalcin@yale.edu); [nikhil.malvankar@yale.edu](mailto:nikhil.malvankar@yale.edu)

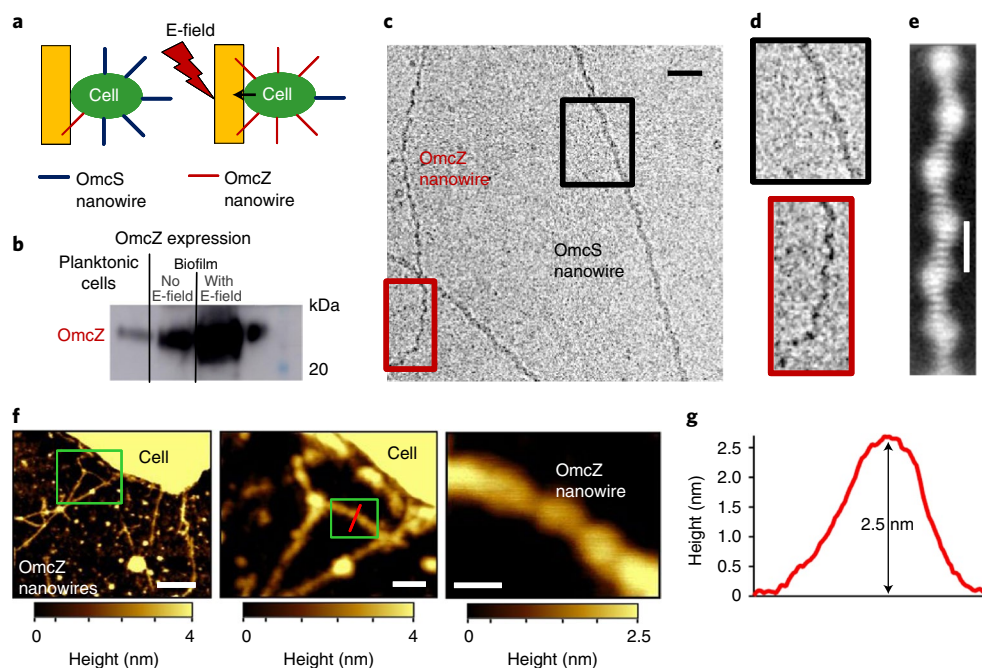


**Fig. 1 | Electric field stimulates production of OmcZ nanowires.** **a**, Schematics of microbial fuel cells for biofilm growth. A detailed setup is shown in Extended Data Fig. 2a. **b**, Immunoblotting showing comparison of OmcZ abundance in filament preparations of WT cells under three different growth conditions. **c**, Cryo-EM images of OmcS (black square) and OmcZ nanowires (red square). Scale bar, 20 nm. **d**, Enlarged images of OmcS and OmcZ nanowires at locations shown in **c**. **e**, Cryo-EM projection (two-dimensional average) of an OmcZ nanowire. Scale bar, 5 nm. **f**, AFM image of a WT bacterial cell grown under an electric field showing OmcZ nanowires with corresponding enlarged images of OmcZ nanowires at locations shown in green squares. Scale bars, 200 nm (left), 50 nm (center) and 20 nm (right). **g**, AFM height profile of the OmcZ nanowire taken at a location shown by a red line in **f**.

OmcZ nanowires that exhibit 1,000-fold higher conductivity than OmcS nanowires. We also find that a low pH-induced formation of beta sheets in OmcS and OmcZ nanowires improves the stacking of hemes and enhances nanowire conductivity and stiffness.

## Results

**Electric field stimulates production of OmcZ nanowires.** To assess the effect of the electric field on the production of OmcZ nanowires, we grew wild-type (WT) *G. sulfurreducens* on graphite anodes serving as an electron acceptor in a microbial fuel cell<sup>13</sup>, with a continuous supply of fumarate as an alternative, soluble electron acceptor (Fig. 1a and Extended Data Fig. 2a,b). In one case, an electric field was supplied by connecting the anode to the cathode whereas in a control case, the anode was disconnected from the cathode to grow the biofilm at the open circuit potential in the absence of an external electric field. In comparison to planktonic cells, or biofilms grown in the absence of an electric field, biofilms grown in the presence of the electric field showed higher abundance of OmcZ in filament preparations as revealed by both peptide mass spectrometry and immunoblotting (Fig. 1b, Extended Data Fig. 2c–f and Supplementary Fig. 1). Furthermore, cryo-EM showed the presence of ~2.5-nm-diameter filaments in these samples in addition to 3.5-nm-diameter OmcS nanowires (Fig. 1c,d). Analysis of images of these thinner filaments showed substantially different helical parameters (an axial rise of 57 Å and a rotation of 160°) compared to OmcS nanowires (an axial rise of 46.7 Å and a rotation of –83.1°)<sup>4</sup>. By analyzing these helical parameters, we determined a molecular weight of ~30 kDa for the protomer in these filaments (see Methods). This molecular weight is consistent with extracellular OmcZ, whereas intracellular OmcZ is 50 kDa (ref. <sup>8</sup>). All these results show that the electric field, applied to biofilms, induces overexpression of OmcZ and suggest that the ~2.5-nm-diameter filaments observed in cryo-EM images could be made up of OmcZ.

AFM images of WT cells grown under an electric field (Fig. 1f,g), and a  $\Delta omcS$  strain (Extended Data Fig. 1b,c, grown under conditions that overexpress OmcZ<sup>8</sup>) showed filaments of ~2.5 nm in diameter on their surface with height and morphology (Fig. 1g and Extended Data Fig. 1d) similar to those of cryo-EM images (Fig. 1c–e). We further analyzed these 2.5-nm-diameter filaments from multiple strains by performing immunogold labeling with anti-OmcZ antibodies, using both AFM (Extended Data Fig. 3a,b) and negative-stain electron microscopy (TEM) (Extended Data Fig. 3c–f). Only these 2.5-nm-diameter filaments showed the labeling, whereas no labeling was found for filaments of a  $\Delta omcZ$  strain or in the absence of the anti-OmcZ antibody (Extended Data Fig. 3c,e). These studies confirmed that the labeling was specific to 2.5-nm-diameter filaments and revealed that these filaments were made of OmcZ. This substantial difference in thickness between nanowires of OmcZ (~2.5 nm) and OmcS (~3.5 nm)<sup>4</sup> (Extended Data Fig. 4) was used to confirm that nanowires used for IR nanospectroscopy, CP-AFM and nanomechanical studies are the same nanowires characterized by cryo-EM and immunogold labeling.

We also analyzed the 2.5-nm-diameter filaments of a ‘W51W57’ mutant bacterial strain where phenylalanine and tyrosine at location 51 and 57, respectively, in the PilA protein were replaced with tryptophan (W) residues<sup>14</sup>. These filaments also showed labeling with anti-OmcZ antibodies (Extended Data Fig. 3a,b,f). Immunoblotting and mass-spectrometry analysis of filament preparations revealed that the W51W57 strain produced more OmcZ than WT (Extended Data Fig. 2c–f). Our finding that the strain W51W57 produces more OmcZ is also consistent with previous studies<sup>15,16</sup> that *pilA* deletion affects the extracellular expression of both OmcS and OmcZ.

**IR nanospectroscopy confirms identity of OmcZ nanowires.** To further determine the composition of individual nanowires, we visualized their protein secondary structure by imaging the

characteristic variations in the line shape of the IR-active amide I vibrational mode (primarily C=O stretch, 1,600–1,700  $\text{cm}^{-1}$ )<sup>17</sup> (Extended Data Fig. 5a,b). IR *s*-SNOM provides quantitative information on the secondary structure for comparisons of different proteins under various environments, although the measured amount of each secondary structure can differ from the amounts of secondary structure in the cryo-EM structure due to SNOM sensitivity toward C=O versus N–H stretch<sup>12</sup> (Extended Data Fig. 6c). Previously, we used IR *s*-SNOM-based nanoscopic chemical imaging to directly visualize water molecules as they bind to individual minerals<sup>18</sup>. Here, to evaluate the reliability and accuracy of our imaging platform for protein structure determination, we first performed IR *s*-SNOM imaging and spectroscopy of two proteins with well-known structures: bacteriorhodopsin<sup>12,19</sup> and lysozyme<sup>17</sup> as well as on individual OmcS nanowires at pH 10.5 (conditions used to solve their atomic structure<sup>4</sup>, Extended Data Figs. 5 and 6). As expected<sup>12,19</sup>, the bacteriorhodopsin exhibited purely  $\alpha$ -helical spectra, indicated by a single peak at 1,663  $\text{cm}^{-1}$  (Extended Data Fig. 5e)<sup>17</sup> while lysozyme showed not only the  $\alpha$ -helical peak but also two additional peaks at 1,618 and 1,678  $\text{cm}^{-1}$  indicative of  $\beta$ -sheets<sup>17</sup> (Extended Data Fig. 6a,b)<sup>17</sup>. Notably, for lysozyme, the relative numbers of  $\alpha$ -helices versus  $\beta$ -sheets measured by IR *s*-SNOM were comparable to those obtained by bulk FTIR, in good agreement with the literature<sup>20</sup> (Extended Data Fig. 6a,b and Supplementary Table 1a). At pH 10.5, the pH used to solve the cryo-EM structure of OmcS<sup>4</sup>, the IR *s*-SNOM images and spectra of OmcS nanowires showed an  $\alpha$ -helical component with the remainder being loop region showing coils and turns (Extended Data Fig. 6c,d). These results were in agreement with the cryo-EM structure of OmcS (Protein Data Bank (PDB) ID 6EF8)<sup>4</sup> that showed largely turns and coils with only 12% helices and 6%  $\beta$  strands<sup>4</sup> (Extended Data Fig. 6c). Together, these studies validate our nanoscale imaging approach for visualization and quantification of protein secondary structure.

At pH 7, by IR *s*-SNOM, OmcS nanowires exhibited an  $\alpha$ -helical component and coil/turns (Fig. 2a,b and Supplementary Table 1b), in agreement with previous studies of the secondary structure of purified OmcS monomers<sup>21</sup>. In contrast, OmcZ nanowires showed a substantial number of  $\beta$ -sheets and little coils/turns (Fig. 2c and Supplementary Table 1b), consistent with previous secondary-structure studies of purified OmcZ monomers<sup>3</sup>. Taken together, IR *s*-SNOM studies, combined with cryo-EM, mass spectrometry, immunoblotting and immunogold labeling show that the electric field applied to biofilms stimulate the production of OmcZ nanowires. As the electric field is strongest near the electrode interface and decreases away from the electrode, OmcZ expression is expected to be maximum at the biofilm–electrode interface. This could explain previous experiments that found that cells show maximum accumulation of OmcZ<sup>10</sup> and highest metabolic activity<sup>22</sup> near the biofilm–electrode interface.

**OmcZ nanowires are 1,000-fold more conductive than OmcS.** To determine the electronic conductivity along individual nanowires, we placed nanowires across a gold–silicon dioxide ( $\text{SiO}_2$ ) interface with the AFM tip being held in contact with an isolated nanowire at various distances away from the gold electrode (Fig. 3a). The current along the nanowire was measured as a function of the DC bias applied between the tip and the gold electrode as a function of nanowire length to determine the contact-free, intrinsic electrical resistance and hence conductance (Fig. 3b). Control measurements by touching the tip directly to gold or insulating  $\text{SiO}_2$  surface yielded expected results, demonstrating the validity of our approach (Supplementary Fig. 2). The resistance of OmcZ nanowires increased linearly with nanowire length, indicative of a wire-like behavior<sup>23</sup> (Fig. 3c). The OmcZ nanowires showed 1,000-fold higher conductivity than OmcS at pH 7 (Fig. 3d), which could explain the ability of cells to transport electrons over 100  $\mu\text{m}$  in biofilms<sup>7</sup>.

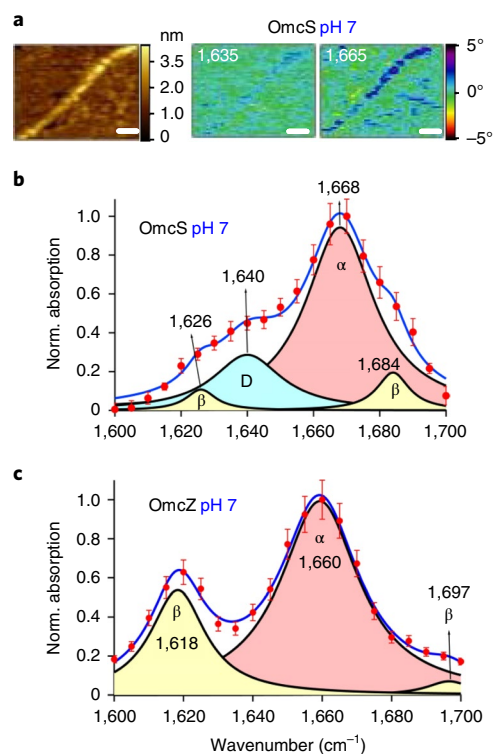


**Fig. 2 | IR nanospectroscopy confirms OmcZ nanowires in biofilms grown under electric field.** **a**, Representative AFM height and corresponding IR *s*-SNOM images with laser excitation at 1,635 and 1,665  $\text{cm}^{-1}$  for OmcS nanowires at pH 7. Scale bar, 0.5  $\mu\text{m}$ . **b,c**, IR nanospectroscopy of amide I at pH 7 for OmcS nanowires (**b**) and OmcZ nanowires (**c**). Blue curves, amide I band-decomposition fits to the data (red markers).  $\alpha$ ,  $\alpha$ -helices;  $\beta$ ,  $\beta$ -sheets; D, loop regions showing coils and/or turns. For **b,c**, data represent mean  $\pm$  s.d. for individual nanowires ( $n = 3$  biologically independent samples).

**Improving  $\pi$ -stacking of hemes increases conductivity.** Grazing-incidence micro-XRD (GI $\mu$ XRD) patterns of OmcZ nanowires showed a more intense peak than OmcS nanowires with  $d$  spacing of 3.6  $\text{\AA}$  (Fig. 4a,b). This  $d$  spacing likely corresponds to the face-to-face  $\pi$ -stacking distance between parallel-stacked hemes, as suggested by the structure of OmcS nanowires (Fig. 4a, inset)<sup>4</sup>. Improved  $\pi$ -stacking increases the effective conjugation length, yielding a longer mean free path for electrons that enhances conductivity<sup>24</sup>. Therefore, our structural analysis indicated that the enhanced conductivity of OmcZ nanowires results from increased crystallinity and reduced disorder within the nanowires (Fig. 4b).

We built a computational model of OmcZ structure to understand the molecular mechanism underlying the increased stacking of hemes in OmcZ as compared to OmcS (Fig. 4 and Supplementary Dataset). Based on the finding that many heme proteins show similar stacking arrangements of hemes<sup>25</sup> (Extended Data Fig. 7b), we used this arrangement of eight hemes as a template for the OmcZ model, which agreed well with the cryo-EM density map for OmcZ nanowires (Fig. 4d). These eight-heme protein structures<sup>25</sup> revealed a dense packing and a substantially different arrangement of hemes when compared to OmcS nanowires (Fig. 4c). This dense packing of hemes is consistent with eight hemes packed in the 30-kDa OmcZ protomer versus six hemes packed in the 45-kDa OmcS protomer (Fig. 4c). Comparison of edge-to-edge heme–heme distances showed that OmcS has only two heme pairs within  $\pi$ -stacking distance (3.5–4  $\text{\AA}$ )<sup>26</sup> whereas the eight-heme protein structures showed five heme pairs within  $\pi$ -stacking distance (Fig. 4c,d and



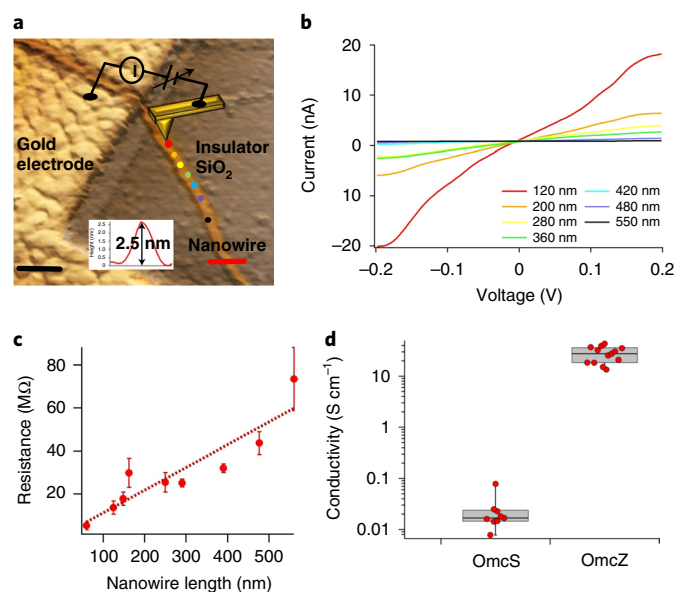


**Fig. 3 | OmcZ nanowires show 1,000-fold higher conductivity than OmcS nanowires.** **a**, Schematic of CP-AFM with AFM topography image of OmcZ nanowire across the gold-SiO<sub>2</sub> interface. Scale bar, 100 nm. Inset, height profile of the nanowire at the red line. **b**, Representative current-voltage (*I*-*V*) curves measured at locations on OmcZ nanowire shown in **a**. **c**, Resistance of OmcZ nanowire as a function of distance away from gold electrode. Dotted line is a linear fit. Data represent mean  $\pm$  s.d. ( $n=8$  measurements for each nanowire length over three biologically independent samples). **d**, Comparison of conductivity of OmcZ versus OmcS nanowires measured using CP-AFM at pH 7. Data represented as a box plot (biologically independent nanowires,  $n=13$  for OmcZ and  $n=9$  for OmcS). The box for the plot was defined as 25 and 75% with center line as median and the whiskers as 10 and 90%.

Supplementary Table 2). These eight-heme protein structures are thus consistent with the XRD data and further indicate that the increased conductivity of OmcZ nanowires is due to a more compact molecular structure with a higher density of heme groups, compared to OmcS nanowires (Fig. 4c,d). The polymerization of OmcZ monomer could further reduce the distance between hemes for closer stacking of hemes in OmcZ nanowires than that found in the OmcS nanowires. In contrast to the OmcS nanowire structure, the OmcZ model showed a  $\beta$ -sheet-rich structure (Fig. 4e,f and Extended Data Fig. 7), in agreement with IR *s*-SNOM studies (Fig. 2). To further evaluate the validity of the OmcZ model, we compared the heme ligation by two consecutive histidines in OmcZ to three different structures of cytochrome c3 (PDB 1GYO, 2BQ4 and 2E84). The amino acid sequence of c3 contains a CXXCHH motif with one proximal and one distal histidine in the heme pairs, while OmcZ contains two distal histidines. All four structures showed consecutive histidines causing tight heme T junctions with similar heme-heme distances (Extended Data Fig. 7e-h).

**Conformation change increases conductivity and stiffness.** We previously found that the conductivity of *G. sulfurreducens* nanowires increases at lower pH<sup>7,14,27,28</sup>, but the underlying mechanism remains unknown<sup>28</sup>. Here, we find evidence of pH-induced structural changes that correlate with increased conductivity. AFM imaging revealed that the nanowire diameter decreased from 3.6 to 2.4 nm for OmcS and from 2.5 to 1.5 nm for OmcZ (Fig. 5a, Extended Data Fig. 4). This reduction in nanowire diameter on lowering the pH helps to explain the increased  $\pi$ -stacking of hemes (Fig. 4a,b). Thus, OmcS and OmcZ nanowires undergo very large

conformational changes (due to decrease in diameter by 12 and 10 Å, respectively) that substantially enhance the conductivity (by ten- and 100-fold, respectively, Fig. 5b) and the stiffness (by 2.5- and 1.5-fold, respectively, Fig. 5c and Extended Data Fig. 8). The conformational changes affecting conductivity of synthetic molecules were previously found to remain local and  $<2$  Å, thus yielding at most a tenfold change in conductivity<sup>29-31</sup>. In contrast, OmcZ nanowires show a 10-Å conformational change and 100-fold increase in conductivity. We anticipate that such very large-scale conformational changes, responsible for stereoelectronic effects, could find applications such as switches in memory and logic devices<sup>29-31</sup>.

To further delineate the mechanism underlying the pH-induced conformational changes, we located nanowires via AFM and compared their corresponding IR *s*-SNOM images at pH 7 (Fig. 2) and pH 2 (Fig. 5d,e). IR *s*-SNOM of the OmcS nanowires at pH 7 showed prominent absorption at 1,665 cm<sup>-1</sup>, corresponding to  $\alpha$ -helices (Fig. 2b). The analysis of the amide I band showed 70%  $\alpha$ -helical, 10%  $\beta$ -sheet and 20% coil/turn (Supplementary Table 1b). On lowering the pH to 2, the absorption at 1,625 cm<sup>-1</sup>, which is assigned to  $\beta$ -sheets<sup>17</sup>, increased sevenfold (Fig. 5d and Supplementary Table 1b). Furthermore, the peak at 1,640 cm<sup>-1</sup> corresponding to coil/turn loops disappeared (Fig. 5d) along with a threefold decrease in the  $\alpha$ -helix peak (Fig. 5d and Supplementary Table 1b). Therefore, much of the  $\alpha$ -helical and coil/turn structures in the OmcS nanowires converted to  $\beta$ -sheets at low pH. Consequently, the stiffness of OmcS nanowires increased 2.5-fold to 1 GPa at pH 2, likely due to an increased number of intermolecular hydrogen bonds in the newly formed  $\beta$ -sheets (Fig. 5c,d and Extended Data Fig. 8)<sup>32</sup>. Furthermore, the conductivity increased tenfold to 0.3 S cm<sup>-1</sup> at pH 2 (Fig. 5b). Therefore, the increase in  $\beta$ -sheet structure can account for the reduction in diameter of OmcS nanowires at pH 2 and their increased conductivity as well as stiffness (Fig. 5a-c and Extended Data Figs. 4 and 8).

On lowering the pH from 7 to 2, OmcZ nanowires exhibited a net 10,000-fold higher conductivity (400 S cm<sup>-1</sup>) and fourfold higher stiffness (1.6 GPa) when compared to OmcS nanowires at pH 7 (Fig. 5b,c and Extended Data Fig. 8). IR *s*-SNOM revealed that at pH 7, OmcZ nanowires displayed a sevenfold increase in  $\beta$ -sheets over OmcS nanowires (Fig. 2b,c and Supplementary Table 1b). At pH 2, the  $\beta$ -sheet content in OmcZ nanowires further increased threefold than at pH 7 (Fig. 5e and Supplementary Table 1b). These results suggest that OmcZ nanowires have highly ordered  $\beta$ -sheets that enhance their conductivity and stiffness (Fig. 5b,c) as well as confer a more compact structure than the OmcS nanowires (Figs. 4d,f and 5a).

AFM and IR *s*-SNOM measurements were performed under ambient conditions<sup>33</sup> to maintain the native protein conformation. The measured heights of OmcS and OmcZ nanowires using AFM were consistent with those obtained from cryo-EM (Fig. 1c,d), validating the comparative analysis. To further quantify the conformational changes, we used four additional complementary methods: FTIR, Raman, fluorescence emission spectroscopy and CD (Fig. 6 and Extended Data Figs. 9 and 10). FTIR revealed that lowering the pH induced formation of  $\beta$ -sheets for both OmcS and OmcZ nanowires as evidenced by a red shift in the amide I peak (Extended Data Fig. 9a-c). However, the frequency shift was lower than that probed by IR *s*-SNOM, due to the diffraction-limited resolution of bulk FTIR<sup>12,17</sup>.

Raman spectroscopy of nanowires of the W51W57 strain in the amide I mode showed that  $\alpha$ -helical regions<sup>34</sup> (1,637 cm<sup>-1</sup>) at pH 7 transform into  $\beta$ -sheets<sup>34</sup> (1,665 cm<sup>-1</sup>) at pH 2 (Fig. 6a), consistent with IR *s*-SNOM studies on individual OmcZ nanowires (Fig. 2c). The amide III mode was also sensitive to conformational changes (Fig. 6b). For nanowires of the WT strain, the coil/turn loop region (1,240 cm<sup>-1</sup>) and part of the  $\alpha$ -helical region ( $\sim$ 1,270 cm<sup>-1</sup>) transformed into  $\beta$ -sheets<sup>34</sup> (1,218 cm<sup>-1</sup>) at pH 2



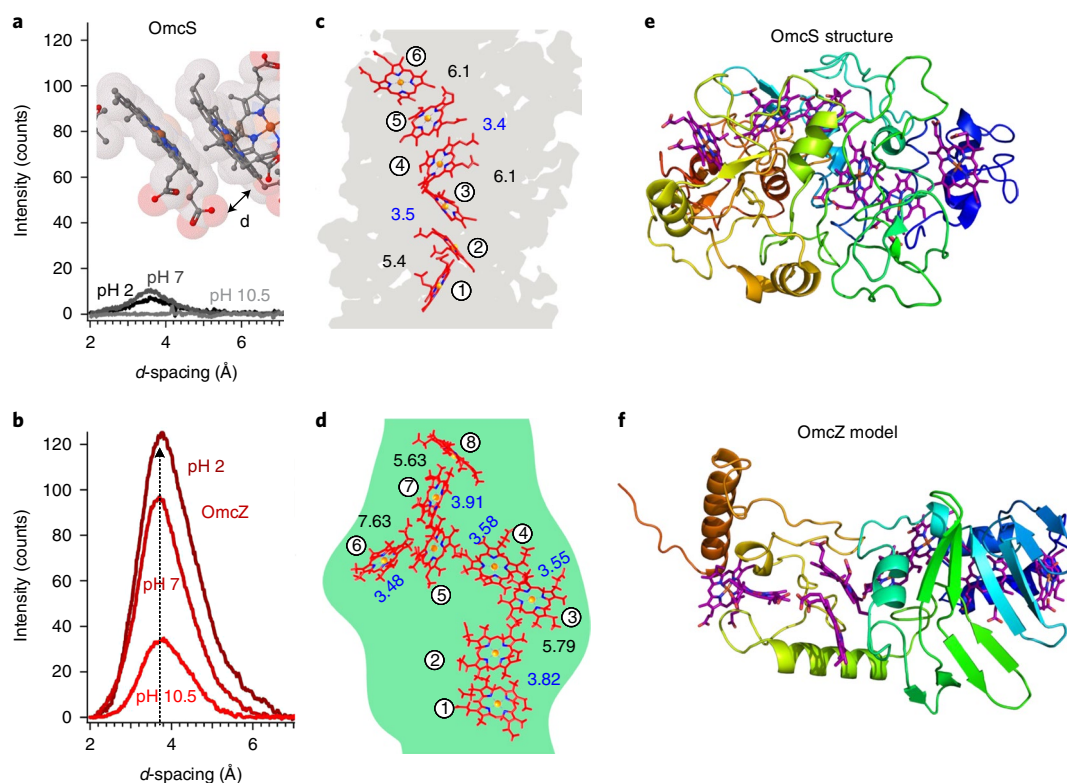


**Fig. 4 | OmcZ nanowires show improved  $\pi$ -stacking between hemes versus OmcS and protonation enhances  $\pi$ -stacking.** **a,b**, GluXRD of OmcS nanowire-containing (**a**) and OmcZ nanowire-containing (**b**) samples revealed increased intensity for a peak at a  $d$  spacing of 3.6 Å (pH 10.5  $\rightarrow$  pH 2) suggesting improved  $\pi$ -stacking between hemes that correlated with enhanced conductivity (see also Fig. 5b). All measurements were repeated multiple times and yielded similar results. Inset for **a**, cryo-EM structure of OmcS nanowire with hemes as stick models colored by chemical elements (gray carbon, blue nitrogen, red oxygen, orange iron), with van der Waals radii translucent. **c,d**, Arrangement of hemes (red) in OmcS (**c**) and eight-heme proteins (**d**). Cryo-EM density is in gray and green for OmcS and OmcZ, respectively. Edge-to-edge distances within the  $\pi$ -stacking range (3.5–4 Å) between heme pairs in OmcS nanowire and eight-heme proteins are in blue. **e**, Cryo-EM structure of OmcS. **f**, Computational model of OmcZ monomer. Coordinates are available in the Supplementary Dataset. Structures in **e** and **f** are colored by residue number, blue N terminus to red C terminus.

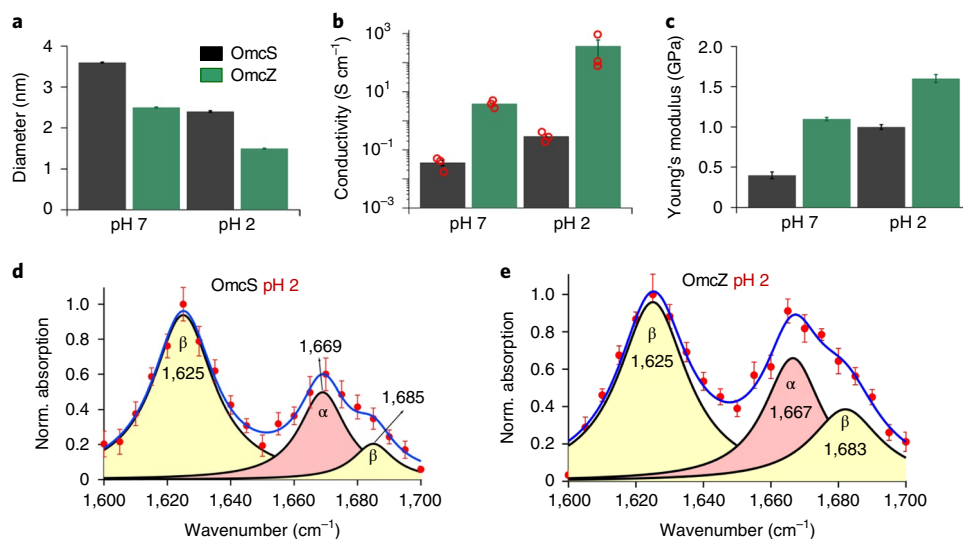


**Fig. 5 | Nanoscale IR spectroscopy establishes pH-induced structural transition in OmcS and OmcZ nanowires.** **a–c**, Relative heights and pH-induced reduction in nanowire diameter (**a**), height-corrected electronic conductivity (**b**) and stiffness (**c**) of OmcS and OmcZ nanowires. Data represent mean  $\pm$  s.d.,  $n=100$  nanowire measurements over three biological replicates for **a** and **c** and mean  $\pm$  standard error of the mean (s.e.m.),  $n=3$  biological replicates for **b** overlaid as red circles. **d,e**, IR nanospectroscopy at pH 2 for OmcS (**d**) and OmcZ (**e**) nanowires. Blue curves, amide I band-decomposition fits to the data (red markers).  $\alpha$ ,  $\alpha$ -helices;  $\beta$ ,  $\beta$ -sheets; D, loop regions showing coil/turns. Data represent mean  $\pm$  s.d. for individual nanowires ( $n=3$  biologically independent samples).

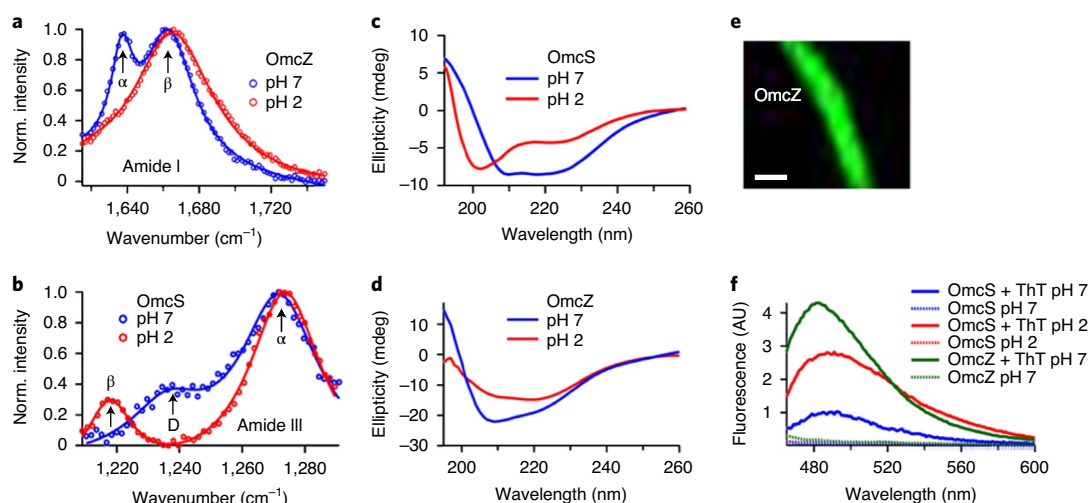


**Fig. 6 | Raman, CD and fluorescence spectroscopy further demonstrates pH-induced structural transition in OmcS and OmcZ nanowire-containing WT and W51W57 samples, respectively. a,b,** Raman spectra at pH 7 and pH 2 for OmcZ nanowires (**a**; amide I) and OmcS nanowires (**b**; amide III) showing transition to  $\beta$  sheets. **c,** CD spectra of OmcS indicating that the predominantly  $\alpha$ -helical structure at pH 7 (blue curve) transforms into  $\beta$ -sheets at pH 2 (red curve). **d,** CD spectra of OmcZ reveal a  $\beta$ -sheet at both pH 7 and pH 2. **e,** Fluorescence microscopy of thioflavin T (ThT)-stained OmcZ nanowires at pH 7. Scale bar, 500 nm. **f,** Fluorescence emission of OmcZ increases threefold at pH 2 with ThT, which binds  $\beta$ -sheets and yields fluorescence enhancement around 485 nm on excitation with a 440-nm laser. All data were background subtracted and were repeated multiple times, yielding similar results.

(Fig. 6b), consistent with IR *s*-SNOM studies on individual OmcS nanowires (Figs. 2b and 5d).

In addition, the CD spectra of WT nanowires at pH 7 displayed the characteristic  $\alpha$ -helical structure<sup>35</sup> with minima near 208 and 222 nm (Fig. 6c) in agreement with OmcS nanowire structure<sup>4</sup>. At pH 2, the intensity at both absorption minima decreased (Fig. 6c), indicating lower  $\alpha$ -helical content. A new absorption minimum appeared at 204 nm (Fig. 6c), consistent with higher  $\beta$ -sheet content<sup>35</sup>. In contrast, nanowires of the W51W57 strain had high  $\beta$ -sheet content at both pH 7 and pH 2 (Fig. 6d), in agreement with our IR *s*-SNOM studies on individual OmcZ nanowires (Figs. 2c and 5e). The numbers of  $\alpha$ -helices and  $\beta$ -sheets quantified with CD Pro (CDSSTR method)<sup>35,36</sup> were consistent with the IR *s*-SNOM results (Supplementary Table 1c). Purified OmcS and OmcZ nanowires from  $\Delta$ omcZ and KN400 strains, respectively, also showed conformational changes similar to nanowires of WT and W51W57 strains (Extended Data Fig. 10 and Supplementary Fig. 3), further confirming that the observed conformational changes are due to nanowires.

We also measured the fluorescence emission near 485 nm of thioflavin T, a  $\beta$ -sheet-specific dye<sup>37</sup>, on binding with nanowires and found homogenous and specific binding (Fig. 6e). Fluorescence emission of nanowire-bound thioflavin T increased by roughly threefold as the pH was reduced from 7 to 2 (Fig. 6f), consistent with the pH-induced  $\beta$ -sheet formation in OmcS nanowires. Nanowires of the W1W57 strain showed high  $\beta$ -sheet content, as evidenced by substantial thioflavin T fluorescence at pH 7 (Fig. 6f), in agreement with studies on OmcZ nanowires (Fig. 2c). These four complementary methods further show the pH-induced structural transition to  $\beta$ -sheets in OmcS and OmcZ nanowires, in agreement with IR *s*-SNOM of individual nanowires (Fig. 5d,e).

## Discussion

Our studies show that OmcZ nanowires confer conductivity to electricity-producing biofilms that could explain high biofilm conductivity even in the absence of OmcS nanowires<sup>7</sup>. Lowering the pH of OmcS and OmcZ nanowires to pH 2 causes a permanent structural transition to a more conductive  $\beta$ -sheet form. Denaturation typically destroys protein function. However, we found that at pH 2, the conductivity of OmcZ nanowires increases 100-fold at pH 2

(Fig. 5b) and nanowires maintain similar morphology (Extended Data Fig. 9g–h). Therefore, it is unlikely that the protein is denatured. Furthermore, the structural change was irreversible, confirming permanent transition to beta sheets at pH 2. Recent studies have emphasized the need for understanding the mechanism of environmentally triggered conformational changes in proteins for the design of protein-based functional materials<sup>38</sup>. Our finding that coil/turns transform into  $\beta$ -sheets in microbial nanowires provides a mechanism for pH-induced conformational changes that reduce their diameter and enhance stiffness and conductivity. Lowering the pH can induce the formation of  $\beta$ -sheets in synthetic peptides<sup>39–41</sup> and the interaction of cytochrome *c* with sodium-dodecyl sulfate (SDS) causes a transition to  $\beta$  sheets<sup>42</sup>. A similar effect could explain the pH-induced formation of  $\beta$ -sheets that reduces the diameter of microbial nanowires.

Another mechanism that could account for the pH-induced reduction of nanowire diameter is a dehydration effect that causes proteins and other polymers to adopt a more compact structure at lower pH<sup>43–45</sup>. In particular, distal histidine coordinating to heme can stabilize the water molecule within the heme pocket by accepting a hydrogen bond<sup>44</sup>. At low pH, the histidine becomes protonated and swings out of the heme pocket, thus destabilizing the water occupancy and leading to dehydration<sup>44</sup>. Additional structural studies will help evaluate these possibilities.

Our findings that highly conductive microbial nanowires contain  $\beta$ -sheets contrast with previous studies that have assumed that nanowires of both *G. sulfurreducens* WT and W51W57 strains are made up of PilA with a purely  $\alpha$ -helical structure<sup>28</sup>. Solution nuclear magnetic resonance studies of the PilA monomer have indicated helical structure even at pH 5 (ref. 28). Therefore, combined with immunogold labeling and cryo-EM, our nanoscopic structural and functional studies suggest that highly conductive microbial nanowires of WT and W51W57 strains are composed of *c*-type cytochromes OmcS and OmcZ and not PilA.

In summary, we have demonstrated the feasibility of manipulating the production and structure of protein nanowires to control their conductivity and stiffness. Our study established the capabilities of multimodal nanospectroscopic approaches for visualizing and quantifying the large-scale conformational

changes in biomolecules. Precise control of electronic and mechanical properties of nanowires can be achieved via targeted environmental changes such as changing the pH, which alters heme stacking or applying an electric field. Previous studies have shown that an electric field can activate a synthetic gene circuit by creating an oxidizing environment<sup>46</sup>. Additional studies are required to evaluate whether a similar mechanism plays a role in these natural systems. Our quantitative method to visualize conformation-induced functional changes is likely applicable to a variety of molecular systems. With OmcZ nanowires displaying a million-fold higher conductivity than synthetic biodegradable materials<sup>1</sup>, we anticipate these new materials will introduce several new features urgently needed for the next generation of bioelectronics, including low cost, ease of synthesis, lack of toxicity, mechanical flexibility, as well as scalable and facile processing with controlled biological properties<sup>1</sup>.

### Online content

Any Nature Research reporting summaries, source data, extended data, supplementary information, acknowledgements, peer review information; details of author contributions and competing interests; and statements of data and code availability are available at <https://doi.org/10.1038/s41589-020-0623-9>.

Received: 13 February 2020; Accepted: 9 July 2020;

Published online: 17 August 2020

### References

1. Someya, T., Bao, Z. & Malliaras, G. G. The rise of plastic bioelectronics. *Nature* **540**, 379–385 (2016).
2. Bathe, M. et al. Roadmap on biological pathways for electronic nanofabrication and materials. *Nano Futures* **3**, 012001 (2019).
3. Zhang, B., Song, W., Brown, J., Nemanich, R. J. & Lindsay, S. Electronic conductance resonance in non-redox proteins. *J. Am. Chem. Soc.* **142**, 6432–6438 (2020).
4. Wang, F. et al. Structure of microbial nanowires reveals stacked hemes that transport electrons over micrometers. *Cell* **177**, 361–369 (2019).
5. Reguera, G. et al. Extracellular electron transfer via microbial nanowires. *Nature* **435**, 1098–1101 (2005).
6. Mehta, T., Coppi, M. V., Childers, S. E. & Lovley, D. R. Outer membrane c-type cytochromes required for Fe(III) and Mn(IV) oxide reduction in *Geobacter sulfurreducens*. *Appl. Environ. Microbiol.* **71**, 8634–8641 (2005).
7. Malvankar, N. S. et al. Tunable metallic-like conductivity in microbial nanowire networks. *Nat. Nanotechnol.* **6**, 573–579 (2011).
8. Inoue, K. et al. Purification and characterization of omcZ, an outer-surface, octaheme c-type cytochrome essential for optimal current production by *Geobacter sulfurreducens*. *Appl. Environ. Microbiol.* **76**, 3999–4007 (2010).
9. Nevin, K. P. et al. Anode biofilm transcriptomics reveals outer surface components essential for high density current production in *Geobacter sulfurreducens* fuel cells. *PLoS ONE* **4**, e5628 (2009).
10. Inoue, K. et al. Specific localization of the c-type cytochrome OmcZ at the anode surface in current-producing biofilms of *Geobacter sulfurreducens*. *Environ. Microbiol. Rep.* **3**, 211–217 (2010).
11. Malvankar, N. S., Tuominen, M. T. & Lovley, D. R. Lack of cytochrome involvement in long-range electron transport through conductive biofilms and nanowires of *Geobacter sulfurreducens*. *Energy Environ. Sci.* **5**, 8651–8659 (2012).
12. Amenabar, I. et al. Structural analysis and mapping of individual protein complexes by infrared nanospectroscopy. *Nat. Commun.* **4**, 2890 (2013).
13. O'Brien, J. P. & Malvankar, N. S. A simple and low-cost procedure for growing *Geobacter sulfurreducens* cell cultures and biofilms in bioelectrochemical systems. *Curr. Protoc. Microbiol.* **43**, A.4K.1–A.4K.27 (2017).
14. Tan, Y. et al. Synthetic biological protein nanowires with high conductivity. *Small* **12**, 4481–4485 (2016).
15. Richter, L. V., Sandler, S. J. & Weis, R. M. Two isoforms of *Geobacter sulfurreducens* PilA have distinct roles in pilus biogenesis, cytochrome localization, extracellular electron transfer, and biofilm formation. *J. Bacteriol.* **194**, 2551–2563 (2012).
16. Liu, X., Zhuo, S., Rensing, C. & Zhou, S. Syntrophic growth with direct interspecies electron transfer between pili-free *Geobacter* species. *ISME J.* **12**, 2142–2151 (2018).
17. Barth, A. Infrared spectroscopy of proteins. *Biochim. Biophys. Acta* **1767**, 1073–1101 (2007).
18. Yalcin, S. E., Legg, B. A., Yeşilbaş, M., Malvankar, N. S. & Boily, J. Direct observation of anisotropic growth of water films on minerals driven by defects and surface tension. *Sci. Adv.* **6**, eaaz9708 (2020).
19. Berweger, S. et al. Nano-chemical infrared imaging of membrane proteins in lipid bilayers. *J. Am. Chem. Soc.* **135**, 18292–18295 (2013).
20. Yang, H., Yang, S., Kong, J., Dong, A. & Yu, S. Obtaining information about protein secondary structures in aqueous solution using Fourier transform IR spectroscopy. *Nat. Protoc.* **10**, 382–396 (2015).
21. Qian, X. et al. Biochemical characterization of purified OmcS, a c-type cytochrome required for insoluble Fe(III) reduction in *Geobacter sulfurreducens*. *Biochim. Biophys. Acta* **1807**, 404–412 (2011).
22. Chadwick, G. L., Otero, F. J., Gralnick, J. A., Bond, D. R. & Orphan, V. J. NanoSIMS imaging reveals metabolic stratification within current-producing biofilms. *Proc. Natl Acad. Sci. USA* **116**, 20716–20724 (2019).
23. Ho Choi, S., Kim, B. & Frisbie, C. D. Electrical resistance of long conjugated molecular wires. *Science* **320**, 1482–1486 (2008).
24. Lee, K. et al. Metallic transport in polyaniline. *Nature* **441**, 65–68 (2006).
25. Valasatava, Y., Andreini, C. & Rosato, A. Hidden relationships between metalloproteins unveiled by structural comparison of their metal sites. *Sci. Rep.* **5**, 9486 (2015).
26. Janiak, C. A critical account on  $\pi$ - $\pi$  stacking in metal complexes with aromatic nitrogen-containing ligands. *J. Chem. Soc., Dalton Trans.* **2000**, 3885–3896 (2000).
27. Adhikari, R., Malvankar, N., Tuominen, M. & Lovley, D. Conductivity of individual *Geobacter* pili. *RSC Adv.* **6**, 8354–8357 (2016).
28. Malvankar, N. S. et al. Structural basis for metallic-like conductivity in microbial nanowires. *mBio* **6**, e00084–00015 (2015).
29. Donhauser, Z. J. et al. Conductance switching in single molecules through conformational changes. *Science* **292**, 2303–2307 (2001).
30. Su, T. A., Li, H., Steigerwald, M. L., Venkataraman, L. & Nuckolls, C. Stereoelectronic switching in single-molecule junctions. *Nat. Chem.* **7**, 215–220 (2015).
31. Li, C., Wang, Z., Lu, Y., Liu, X. & Wang, L. Conformation-based signal transfer and processing at the single-molecule level. *Nat. Nanotechnol.* **12**, 1071 (2017).
32. Simone, R. F. et al. Influence of the  $\beta$ -sheet content on the mechanical properties of aggregates during amyloid fibrillization. *Angew. Chem. Int. Ed.* **54**, 2462–2466 (2015).
33. Freund, J., Halbritter, J. & Hörber, J. How dry are dried samples? Water adsorption measured by STM. *Microsc. Res. Tech.* **44**, 327–338 (1999).
34. Rygula, A. et al. Raman spectroscopy of proteins: a review. *J. Raman Spectrosc.* **44**, 1061–1076 (2013).
35. Sreerama, N. & Woody, R. W. Estimation of protein secondary structure from circular dichroism spectra: comparison of CONTIN, SELCON, and CDSSTR methods with an expanded reference set. *Anal. Biochem.* **287**, 252–260 (2000).
36. Greenfield, N. J. Using circular dichroism spectra to estimate protein secondary structure. *Nat. Protoc.* **1**, 2876–2890 (2006).
37. Guterman, T. et al. Formation of bacterial pilus-like nanofibres by designed minimalistic self-assembling peptides. *Nat. Commun.* **7**, 13482 (2016).
38. Boyken, S. E. et al. De novo design of tunable, pH-driven conformational changes. *Science* **364**, 658–664 (2019).
39. Koga, T., Taguchi, K., Kobuke, Y., Kinoshita, T. & Higuchi, M. Structural regulation of a peptide-conjugated graft copolymer: a simple model for amyloid formation. *Chem.-A Eur. J.* **9**, 1146–1156 (2003).
40. Cerpa, R., Cohen, F. E. & Kuntz, I. D. Conformational switching in designed peptides: the helix/sheet transition. *Fold. Des.* **1**, 91–101 (1996).
41. Cote, Y. et al. Mechanism of the pH-controlled self-assembly of nanofibers from peptide amphiphiles. *J. Phys. Chem. C* **118**, 16272–16278 (2014).
42. Haldar, S., Sil, P., Thangamuniyandi, M. & Chattopadhyay, K. Conversion of amyloid fibrils of cytochrome c to mature nanorods through a honeycomb morphology. *Langmuir* **31**, 4213–4223 (2015).
43. Wang, X., Ye, X. & Zhang, G. Investigation of pH-induced conformational change and hydration of poly (methacrylic acid) by analytical ultracentrifugation. *Soft Matter* **11**, 5381–5388 (2015).
44. Esquerra, R. M. et al. The pH dependence of heme pocket hydration and ligand rebinding kinetics in photodissociated carbonmonoxymyoglobin. *J. Biol. Chem.* **283**, 14165–14175 (2008).
45. Durchschlag, H. & Zipper, P. Modeling the hydration of proteins at different pH values. *Anal. Ultracentrif. VII* **127**, 98–112 (2004).
46. Tschirhart, T. et al. Electronic control of gene expression and cell behaviour in *Escherichia coli* through redox signalling. *Nat. Commun.* **8**, 14030 (2017).

**Publisher's note** Springer Nature remains neutral with regard to jurisdictional claims in published maps and institutional affiliations.

© The Author(s), under exclusive licence to Springer Nature America, Inc. 2020



## Methods

**Bacterial strains and growth conditions.** *G. sulfurreducens* WT strain PCA (designated DL-1) (ATCC 51573, DSMZ 12127)<sup>4</sup>, the *omcS* knock-out mutant strain<sup>6</sup> (designated  $\Delta omcS$ ), the *omcZ* knock-out mutant strain<sup>9</sup> (designated  $\Delta omcZ$ ), the *omcZ* knock-in strain that overexpresses *OmcZ*<sup>47</sup> (designated ZKI), strain W51W57 (ref. <sup>14</sup>) and strain Aro5 (ref. <sup>48</sup>) were obtained from our laboratory culture collection. The cultures were maintained at 30 °C or at 25 °C under strictly anaerobic conditions in growth medium supplemented with acetate (10 mM) as the electron donor and fumarate (40 mM) as the electron acceptor. These strains were grown under electron acceptor-limiting conditions that increases *OmcZ* expression (Fig. 1b and Extended Data Fig. 2e)<sup>13</sup>. We found that *G. sulfurreducens* WT (DL-1) strain primarily makes *OmcS* nanowires whereas strain W51W57 overexpresses *OmcZ* (Extended Data Fig. 2e) and shows abundance of *OmcZ* nanowires (Extended Data Fig. 3a,f). Therefore, unless otherwise noted, the WT strain was used to focus on studies of *OmcS* nanowires whereas the W51W57 strain was used to focus on studies of *OmcZ* nanowires. As described previously<sup>4</sup>, the cells were grown in sterilized and degassed NBAF medium<sup>13</sup> and 1 l of NBAF medium contained the following: 0.04 g l<sup>-1</sup> of calcium chloride dihydrate, 0.1 g l<sup>-1</sup> of magnesium sulfate heptahydrate, 1.8 g l<sup>-1</sup> of sodium bicarbonate, 0.5 g l<sup>-1</sup> sodium carbonate, 0.42 g l<sup>-1</sup> of potassium phosphate monobasic, 0.22 g l<sup>-1</sup> of potassium phosphate dibasic, 0.2 g l<sup>-1</sup> of ammonium chloride, 0.38 g l<sup>-1</sup> of potassium chloride, 0.36 g l<sup>-1</sup> of sodium chloride and vitamins and minerals as listed in ref. <sup>13</sup>. Resazurin was omitted and 1 mM of cysteine was added as an oxygen scavenger. The cells were grown on electrodes under electron acceptor-limiting conditions to induce the expression of *OmcZ* nanowires<sup>13</sup> (Fig. 1a,f).

***G. sulfurreducens* nanowire preparation and biochemical characterization.** As described previously<sup>4</sup>, nanowires were separated from bacteria and extracted via centrifugation<sup>14</sup> and maintained in 150 mM ethanolamine buffer at pH 10.5 in a manner similar to structural studies on bacterial filaments<sup>49</sup>. Cells were gently scraped from the electrode surface using a plastic spatula and isotonic wash buffer (4.35 × 10<sup>-3</sup> M of NaH<sub>2</sub>PO<sub>4</sub>·H<sub>2</sub>O, 1.34 × 10<sup>-3</sup> M of KCl, 85.56 × 10<sup>-3</sup> M of NaCl, 1.22 × 10<sup>-3</sup> M of MgSO<sub>4</sub>·7H<sub>2</sub>O and 0.07 × 10<sup>-3</sup> M of CaCl<sub>2</sub>·2H<sub>2</sub>O), then collected by centrifugation and resuspended in 150 × 10<sup>-3</sup> M of ethanolamine (pH 10.5). Filaments were mechanically sheared from the cell surface using either vortexing for 1 min or a Waring Commercial Blender (catalog no. 7011 S) at low speed for 1 min and then cells were removed by centrifugation at 13,000g before collecting filaments with an overnight 12.5% ammonium sulfate precipitation and subsequent centrifugation at 13,000g for 60 min. Collected filaments were resuspended in ethanolamine buffer and further purified by centrifugation at 23,000g to remove debris and a second 12.5% ammonium sulfate precipitation with centrifugation at 13,000g (ref. <sup>14</sup>). The final filament preparation was resuspended in 200 μl of ethanolamine buffer. Filament preparations were further passed through 0.2-μm filters to remove any residual cells and stored at 4 °C. The pH of the buffer was equilibrated using HCl as previously described<sup>7</sup>. Cell-free filament preparations were imaged first with TEM to ensure sample quality.

**Cell and protein normalization for comparative expression studies.** Bacterial strains were grown to late exponential phase (optical density (OD<sub>600</sub>) ~0.6–0.7) unless specified. For filament preparations, strains were normalized to the initial wet weight of the bacterial pellet. All the steps were performed in parallel and special care was taken to ensure that at each step the pellets were resuspended in same volumes across the strains. Equal volumes (1/20th of the final filament preparation protein) was loaded on the gels for comparison. Additional care was taken to collect the samples at a similar growth phase and optical density when comparing different strains.

**SDS-PAGE.** For polyacrylamide gel electrophoretic separation (SDS-PAGE), the samples were boiled in 2.5% SDS sample buffer that included β-mercaptoethanol for 12 min. The samples were run on a 4–20% gradient protein gel (BioRad) at a constant voltage of 200 V for 30 min. Precision Plus Protein Prestained molecular weight standards (BioRad) and Low Range Protein Ladder (Thermo Scientific) were used to compare the molecular weight of cytochromes in the filament preparations. Gels were immediately washed at least three times with ultra-pure deionized water over a 1-h period, stained with Coomassie R-250 stain (Thermo Scientific) and destained overnight.

**Immunoblotting.** Custom polyclonal anti-*OmcZ* antibody was synthesized by LifeTein by immunizing two rabbits with synthetic peptide sequence (DSPNANLGTVKPGL) containing targeted epitope on the native protein, *OmcZ*, and then affinity purifying the serum against that peptide sequence. The antibody was used at a dilution of 1:5,000 for immunoblotting. Filament preps were normalized to the initial cell mass of the starting material.

**Mass spectrometry.** For liquid chromatography–tandem mass spectrometry analysis of filament preparations, the *OmcZ* band (~30 kDa) was excised from the gel and treated with chymotrypsin to digest the protein. Proteomic analysis of the cleaved peptides from filaments was performed by the Keck Facilities at Yale University. Unique amino acid sequence matches with the *OmcZ* were found

(Extended Data Fig. 2c,d). For quantification of *OmcZ* in filament preparations, the ‘top three’ method<sup>50,51</sup> was used by quantitating the three peptides with highest intensity<sup>52</sup> (Extended Data Fig. 2f). Previous study has confirmed that *OmcZ* contains eight hemes through intact mass spectrometry and pyridine hemochrome assay<sup>6</sup>.

**Estimation of molecular weight of *OmcZ* nanowires using cryo-EM.** Mass of the protein (*M* in kDa) is proportional to its volume due to the fact that most of proteins have intrinsically similar density ~1.35 g cm<sup>-3</sup> (*V* in Å<sup>3</sup>)<sup>53</sup>. Therefore,  $M_1/M_2 = V_1/V_2$  where  $M_1$  and  $M_2$  are the masses for the respective proteins and  $V_1$  and  $V_2$  are their volumes. For *OmcS*,  $M_1 = 47$  kDa and  $V_1$  is computed from the helical parameters as follows: the axial distance between two subunits called rise is 46.7 Å and the axial distance between one helical turn called pitch is 200 Å. Therefore, *OmcS* nanowire has 200/46.7 = 4.28 subunits per helical turn. Volume of *OmcS* filament per helical turn is approximated by  $\pi r^2 L$  where  $r$  is the radius of *OmcS* filament (35/2 = 17.5 Å) and  $L$  is the length (200 Å) that gives a volume of 192,423 Å<sup>3</sup>. As there are 4.28 subunits per turn, the volume of *OmcS* subunit ( $V_1$ ) is 192,423/4.28 = 44,959 Å<sup>3</sup>.

For 2.5-nm-diameter filament, the helical rise is 57 Å and pitch is 128.25 Å, giving 128.25/57 = 2.25 subunits per turn. Volume of these filaments per helical turn using the same equation is  $\pi r^2 L$  where  $r$  is the radius of filament (25/2 = 12.5 Å) and  $L$  is the length (128.25 Å) that gives volume 62,954.7 Å<sup>3</sup>. As there are 2.25 subunits per turn, the volume of the subunit ( $V_2$ ) is 62,954.7/2.25 = 27,980 Å<sup>3</sup>. Therefore, using the relation  $M_2 = M_1 \times V_2/V_1$ , the estimated mass of the protomer of these filaments is 27,980 × 0.001 = 28 kDa, which is close to molecular weight of 30 kDa for extracellular form of *OmcZ*<sup>8</sup>.

**AFM sample preparation.** Before all measurements, nanowires were imaged with AFM and height measurements were performed to confirm the presence of individual nanowires and to confirm their identity. IR s-SNOM measurements were also performed on bundles of *OmcS* nanowires under high pH conditions (pH ≥ 7). These nanowires did not show any β-sheets and the results were similar to individual *OmcS* nanowires showing primarily α-helix as secondary structure, confirming that low pH conditions are necessary to induce the formation of β-sheets in *OmcS* nanowires.

For imaging with AFM or combined AFM and IR s-SNOM or CP-AFM, 20 μl buffer containing nanowires was drop casted onto appropriate substrates. Freshly cleaved mica (Muscovite Grade V1, SPI supplies) was used for topography imaging only whereas template-stripped gold surface (Platypus, AU.1000.SWTS) was used for IR s-SNOM and nanoelectrode gold array was used for CP-AFM. Except mica, all substrates were plasma cleaned for 10 min under medium plasma exposure and washed with deionized water (Fig. 2a). For bulk FTIR, Raman, CD, GI-XRD and fluorescence emission spectroscopy, nanowires were directly measured in their native buffer environment. Conformation change at pH 2 in the films of *OmcS* nanowires in Citrate buffer was similar to phosphate buffer (Extended Data Fig. 9d–f). Therefore, the Citrate buffer was used for height analysis of *OmcS* nanowires.

**Immunogold labeling of *OmcZ* nanowires.** TEM-based immunogold labeling was performed as described previously<sup>10</sup>. In brief, samples of purified extracellular filaments were adsorbed to plasma-cleaned carbon film-coated copper grids (400 mesh, Electron Microscopy Sciences) and incubated for 5–10 min. Samples were subsequently treated with 0.1% glutaraldehyde (supplied as 2.5% Glutaraldehyde in 0.1 M of Sorensen's sodium-potassium phosphate buffer, Electron Microscopy Sciences, and diluted in a 0.2 M solution of the same buffer) followed by rinsing with a Sorensen's buffer solution (0.2 M, pH 7.2, Electron Microscopy Sciences). The grids were then treated for 15 min with 3% bovine serum albumin (BSA) dissolved in Sorensen's buffer, followed by 30 min to 2 h incubation with either the monospecific anti-*OmcZ* antibodies developed for this study (LifeTein) or the previously described peptide-based rabbit-derived polyclonal antibodies against *OmcZ*<sup>8</sup>; for these primary antibody incubations the antibodies were diluted 1:50 in Sorensen's buffer containing 0.3% BSA. Grids were then rinsed three times in Sorensen's buffer solution and incubated for 30 min to 1 h with goat-derived polyclonal secondary antibodies conjugated to gold nanoparticles (6 or 12 nm Colloidal Gold AffiniPure Goat Anti-Rabbit IgG (H + L) (EM Grade), Jackson ImmunoResearch Laboratories, Inc.). Grids were then rinsed three times in Sorensen's buffer solution and negatively stained with 1% phosphotungstic acid (pH 6.8) for 15 to 30 s and subsequently air-dried. Finally, grids were examined using a JEOL JEM-1400 Plus transmission electron microscope operated at 80 kV. Immunogold samples imaged via AFM (Extended Data Fig. 3a) were prepared as above, except that samples were adsorbed to a mica substrate rather than TEM grids and no negative staining solution was applied.

**Bacteriorhodopsin (bR) preparation.** The bR from *Halobacterium salinarum* (Sigma Aldrich B0184, native sequence, lyophilized powder) was diluted to a stock concentration of ~150 μg ml<sup>-1</sup> in 0.01% sodium azide (NaN<sub>3</sub>). Adsorption buffer (20 μl, 150 mM of KCl + 10 mM of Tris/HCl at pH 7.4) was drop casted onto the gold surface and 20 μl of stock bR were added to the droplet. After ~30 min, the sample was rinsed with deionized water.

**Lysozyme preparation.** Lysozyme was purified from chicken egg white (Sigma Aldrich L7651) and dissolved in 10 mM of potassium phosphate ( $\text{KH}_2\text{PO}_4$ ) buffer at pH 7 (final concentration  $\sim 200 \mu\text{g ml}^{-1}$ ). The lysozyme sample was prepared similar to the procedure described for bR.

**AFM of nanowires and other proteins.** AFM experiments for height measurements were performed using soft cantilevers (AC240TSA-R3, Oxford Instrument Co.) with a nominal force constant of  $2 \text{ N m}^{-1}$  and resonance frequencies of 70 kHz. The free-air amplitude of the tip was calibrated with the Asylum Research software and the spring constant was captured by the thermal vibration method. Samples were imaged with a Cypher ES scanner using intermittent tapping (AC–air topography) mode. All nanowires height analyses and statistics were performed using Gwyddion and IGOR Pro software (WaveMetrics, Inc.). To check protein quality for IR nanospectroscopy, AFM was performed using cantilevers (Arrow-NCR, Nano Worlds) with a nominal force constant of  $42 \text{ N m}^{-1}$  and a resonance frequency of 285 kHz. Samples were imaged with an Icon AFM (Bruker) using intermittent tapping (AC–air topography) mode. Liquid AFM was performed using bio-lever mini tips (BL-AC40TS, Olympus) with resonance frequency of 25 kHz in liquid and nominal force of  $0.1 \text{ N m}^{-1}$ . AFM images were processed using the Gwyddion package.

**Nanoelectrode design and fabrication.** Electrodes made of gold separated by a nonconductive gap (Fig. 3a) were designed using electron-beam lithography. Interdigitated electrode devices were designed in Layout Editor, a computer-aided design program. The electrodes were patterned by electron-beam lithography on a sacrificial electron-beam resist layer spin coated onto a 300 nm layer of insulating silicon dioxide ( $\text{SiO}_2$ ) grown on a silicon wafer. The wafer was then developed in a solution of cooled isopropyl alcohol to remove the resist layer where the pattern was printed. A 30-nm-thick gold film was evaporated after a 5-nm-thick titanium adhesion layer on lithographically patterned wafer using an electron-beam evaporator (Denton Infinity 22). The electron-beam resist was removed with *N*-methyl-2-pyrrolidone by incubating for 15–20 min at  $80^\circ\text{C}$  until the lift-off was complete. The device was then rinsed sequentially with acetone, methanol and isopropanol before being dried with nitrogen, resulting in gold nanoelectrodes with a nonconductive gap (Fig. 3a). All device fabrication was performed in a class 1,000 cleanroom to avoid contamination. The devices were further inspected with optical and scanning electron microscopy to ensure that the electrodes are well separated by a nonconductive gap, and resistance measurements were used to confirm that the electrodes are well insulated from each other ( $R_{\text{gap}} > 1 \text{ T}\Omega$ ). Before usage, the device was washed with distilled water and then rinsed with isopropanol to remove contaminants on the surface. The device was further cleaned for 1 min with oxygen plasma and dried with nitrogen flow.

**IR s-SNOM on individual proteins.** As described previously<sup>18</sup>, we used IR radiation from a wavelength-tunable quantum cascade laser (Daylight Solutions MIRcat Amide quantum cascade laser tunable from 1,450 to  $1,700 \text{ cm}^{-1}$  with a bandwidth  $< 1 \text{ cm}^{-1}$  and spectral resolution of  $0.25 \text{ cm}^{-1}$ ) to illuminate a conductive AFM tip with  $< 20 \text{ nm}$  spatial resolution (Extended Data Fig. 5a,b). We incorporated this IR-coupled AFM to one arm of a Michelson interferometer and focused the IR laser to the AFM tip apex with a parabolic mirror (numerical aperture (NA), 0.25 and power of  $< 10 \text{ mW}$ ) (Extended Data Fig. 5a). We used conductive PtSi (PtSi-NCH, Nanosensors) with a tip radius of  $\sim 20 \text{ nm}$  operating in tapping mode (resonance frequency  $\omega_t \approx 330 \text{ kHz}$ ). We operated the interferometer in two-phase homodyne mode for IR s-SNOM<sup>19</sup> to isolate and amplify the near-field, tip-scattered signal from the far-field background. We tuned the laser from 1,600 to  $1,700 \text{ cm}^{-1}$  in  $5 \text{ cm}^{-1}$  steps and recorded images at each wavenumber to obtain the amide I spectra using IR s-SNOM. IR s-SNOM phases describe absorption properties. For background subtraction, we obtained the phases from the sequential images from the empty region on the gold substrate (Extended Data Figs. 5 and 6)<sup>19</sup>.

The tip-scattered IR radiation was recombined with the reference field for two-phase ( $\Phi_1$  and  $\Phi_2$  in Extended Data Fig. 5a) homodyne amplification and detection with a HgCdTe detector (Kolmar Technologies). Far-field background was suppressed by demodulating the detected signal with lock-in amplifier (Zurich Instruments, HF2LI) at third harmonic of the cantilever oscillation frequency ( $3\omega_t$ ) except for bR that used  $3\omega_t + \Omega$ , where  $\Omega$  is the frequency of the chopper used in the reference arm<sup>19</sup>. This modulation scheme isolated the near-field signal and provided the background-free near-field phase  $\phi$ . Extracted near-field phase signals were used to access the absorptive properties of imaged proteins. Raster scanned s-SNOM images were acquired with a lock-in time constant of 10 ms per pixel that yielded good near-field signal contrast and avoided sample drift. The signal from the gold was at least ten times lower than intrinsic protein signal, ensuring a high signal-to-noise ratio to extract the protein structure. All IR s-SNOM analyses and statistics were performed using Gwyddion software (Figs. 2 and 5 and Extended Data Figs. 5 and 6).

To extract near-field phase (absorption) properties of proteins, we used a two-phase homodyne detection technique by changing the reference arm between two orthogonal known phase components such as  $\Phi_1 = \Phi_2 + \pi/2$  and extracted near-field amplitude and phase signal using following relations:<sup>18,19</sup>

$$I_1 = A \cos(\Phi - \Phi_1), \text{ using } \Phi_1 = \Phi_2 + \pi/2$$

$$I_2 = A \cos(\Phi - \Phi_2) = A \sin(\Phi - \Phi_1)$$

$$\text{Near - Field Phase : } \Phi_{\text{NF}} = \arctan(I_1/I_2)$$

where  $I$  is the intensity and  $A$  is a constant. Nanoscale IR spectroscopy studies have demonstrated sensitivity to detect beta sheets in a wide range of proteins such as insulin<sup>12</sup>, tobacco mosaic virus<sup>12</sup>, silk<sup>24</sup>,  $\beta_2$ -microglobulin<sup>25</sup>, diphenylalanine<sup>26</sup>, Josephin domain of ataxin-3 amyloid<sup>27</sup> and Huntingtin protein<sup>28</sup>.

**Deconvolution and peak fitting of amide I spectra for IR s-SNOM and bulk FTIR.** Band-decomposition analysis was conducted using a multipeak fitting analysis program (IGOR Pro, WaveMetrics, Inc.). IR s-SNOM spectra were evaluated with Lorentzian line shapes<sup>19</sup> and bulk FTIR spectra were evaluated with Gaussian line shapes<sup>20</sup>. For IR s-SNOM of nanowires, bR and lysozyme, data are represented with red markers. Fitting results (blue curves) were obtained by applying band-decomposition analysis to the data, which yielded good agreement ( $\chi^2 < 0.02$ ). Areas under the curve were integrated to estimate the percentages of  $\alpha$ -helix,  $\beta$ -sheet and coil components (Supplementary Table 1a for lysozyme and Supplementary Table 1b for OmCS and OmCZ nanowires). In amide I mode,  $\alpha$ -helices give rise to main absorption band located at  $1,660 \text{ cm}^{-1}$ .  $\beta$ -sheets show a stronger band at  $1,625 \text{ cm}^{-1}$  and a weaker band near  $1,685 \text{ cm}^{-1}$ ,  $\sim 60 \text{ cm}^{-1}$  away from the stronger band<sup>17</sup>. This observed splitting in the  $\beta$ -sheet formation arises due to the transition dipole coupling mechanism<sup>17</sup>. The formation of  $\beta$ -sheets in IR s-SNOM spectra for OmCS and OmCZ nanowires was evident from the presence of these two  $\beta$ -sheet bands<sup>17</sup> (Fig. 5d,e). All analyses were performed using IGOR Pro software (WaveMetrics, Inc.).

**CP-AFM measurements.** To measure the conductivity of nanowires using CP-AFM,  $5 \mu\text{l}$  of ethanolamine buffer solution containing nanowires were deposited on gold electrodes patterned with electron-beam lithography on a silicon wafer grown with 300 nm silicon dioxide as described above. The excess buffer was absorbed with filter paper. After air-drying, the sample was mounted on a metal puck and transferred to the sample stage inside the AFM (Oxford Instrument Co., Cypher ES). AFM and subsequent CP-AFM experiments were performed using soft cantilevers (ASYELEC-01, Oxford Instruments) with a nominal force constant of  $2 \text{ N m}^{-1}$  and resonance frequencies of 70 kHz. The tip was coated with Pt–Ir. The free-air amplitude of the tip was calibrated with the Asylum Research software and the spring constant was captured by the thermal vibration method. For CP-AFM experiments, the dual gain ORCA holder was used (Asylum Research) to record both low and high current values. The sample was imaged with a Cypher ES scanner using intermittent tapping (AC–air topography) mode. AFM showed that gold electrodes were partially covered with nanowires to facilitate CP-AFM measurements (Fig. 3a). After identifying OmCZ nanowires across the electrodes and the substrate, the tip was withdrawn and brought into contact with the nanowires by switching on the contact mode. Points along the length of the nanowires were selected based on the AFM image (Fig. 3a) and the corresponding distance was measured with Asylum Research software that is used to operate AFM. With partially gold-coated substrate as the first electrode and a metal-coated AFM tip as a second mobile electrode, the uncovered parts of the nanowires were electrically contacted, measuring the  $I$ – $V$  characteristics as a function of the distance between the tip and the electrode by applying a bias ramp in the range of  $-0.2$  to  $+0.2 \text{ V}$  (Fig. 3b), and then the tip was withdrawn to the next point. To verify proper electrical contact during the measurements, the tip was frequently brought into contact with either gold or  $\text{SiO}_2$  substrate (Supplementary Fig. 2). A loading force of  $50 \text{ nN}$  was used to obtain stable current and the same force was used for all experiments reported in this manuscript. The  $I$ – $V$  characteristics were captured in the software and the analysis was conducted in IGOR Pro software (WaveMetrics, Inc.).  $I$ – $V$  curves were processed using the 75 points Savitzky–Golay smoothing function before fitting using IGOR Pro software (WaveMetrics, Inc.). The linear regime of the  $I$ – $V$  characteristics was used for calculation of resistance using the equation:  $R = V/I$ . The resistance from different points was then plotted as a function of distance ( $L$ ) (Fig. 3c). For each distance, at least eight repeats were recorded and a minimum of three biological replicates were used to evaluate statistical significance (Fig. 3c,d).

**Conductivity calculations.** The conductivity ( $\sigma$ ) of nanowires (Figs. 3d and 5b) was calculated using the relation  $\sigma = G \times (L/A)$  where  $G$  is the conductance measured previously<sup>14</sup> that is reciprocal of resistance  $R$ ,  $L$  is the length of the nanowire and  $A = \pi r^2$  is the area of cross section of the nanowire with  $2r$  as the height of the nanowire measured using AFM, taking into account pH-induced reduction in diameter (Fig. 5a and Extended Data Fig. 4). Due to the extremely small ( $\sim 3 \text{ nm}$ ) height of the nanowires, the small cross-sectional area of the nanowires gives rise to higher conductivity. Note that these height-corrected values (Fig. 5b) are a lower estimate for the conductivity of individual nanowires compared to that measured directly using conducting-probe AFM (Fig. 3d).

As our W51W57 cell growth and filament preparation conditions were similar to previous studies<sup>14</sup>, our results suggest that the nanowires reported to

be tryptophan-substituted pili<sup>14</sup> are OmcZ nanowires and hence were used for conductivity comparison with OmcS (Fig. 5b).

**Stiffness measurements.** The OmcS and OmcZ nanowires were prepared for stiffness measurements in a manner similar to AFM sample preparation described earlier. Samples were imaged with a Cypher ES scanner using amplitude modulation–frequency modulation bimodal imaging mode using Arrow UHFAuD (Nanoworld) cantilever with 6 N m<sup>−1</sup> nominal force constant ( $k_1$ ). The spring constant for both the first and second eigenmodes ( $k_1$  and  $k_2$ ) and the quality factor ( $Q$ ) of the tip was calibrated by fitting the thermal vibration curves before the experiment. To operate in bimodal amplitude modulation–frequency modulation imaging mode, the tip was tuned on both eigenmodes before tip sample interaction. Tuning of the cantilever was modulated with the blue drive aligned to the base of the cantilever to produce maximum driving power. The first cantilever eigenmode was excited to the resonant frequency ( $f_1 \approx 2$  MHz) and tuned with the AFM software (Asylum Research) and the second eigenmode was excited to the second-order resonant frequency ( $f_2 \approx 7$  MHz) at least  $\sim 100$  times lower in amplitude than the first eigenmode.

On approaching the sample, the tip was final tuned to compensate for the shift in drive frequency induced by tip sample interaction. Repulsive imaging mode was used (phase  $< 90^\circ$ ) to overcome adhesion force. Drive amplitude was adjusted to maintain a small indentation depth ( $\sim 300$  pm) and the maximum indentation depth  $\delta$  was monitored from the imaging feedback loop using the following relation:

$$\delta = \frac{3}{4} \left( \frac{k_1}{Q_1} A_{1,\text{free}} \cos \phi_1 \right) \left( \frac{2k_2 \Delta f_2}{f_2} \right)^{-1}$$

where  $A_{1,\text{free}}$  is the free amplitude tuned for the first eigenmode,  $\phi_1$  is the phase response of the first eigenmode and  $\Delta f_2$  is the frequency shift monitored from the second eigenmode. The effective storage modulus of the interaction  $E_{\text{eff}}$  was calculated from the following equation using a Hertz punch model:<sup>29</sup>

$$E_{\text{eff}} = \frac{\pi}{R} \sqrt{\frac{1}{6} \left( \frac{k_1}{Q_1} \frac{A_{1,\text{free}}}{A_{1,\text{set}}} \cos \phi_1 \right)^{-1} \left( \frac{2k_2 \Delta f_2}{f_2} \right)^{\frac{2}{3}}}$$

where  $A_{1,\text{set}}$  is the setpoint used for imaging and  $R$  ( $\sim 7$  nm) is the tip radius provided by the manufacturer. Correlated topography and Young's modulus images were generated with a resolution of  $512 \times 512$  pixels (Extended Data Fig. 8). The mean value of the nanowire modulus was extracted by fitting a Gaussian function to the histograms created from the modulus map of three biological replicates (Extended Data Fig. 8). The same tip and imaging configuration were used for all samples to maintain consistency between measurements.

**GIpXRD.** To visualize the stacking of hemes in nanowires and to investigate the effect of pH on the stacking, GIpXRD data were collected in grazing-incidence mode using a Rigaku D/Max Rapid II instrument equipped with a two-dimensional image plate detector. The Arco5 strain was used to focus on OmcS nanowires whereas W51W57 strain was used to probe OmcZ nanowires. X-rays were generated by a MicroMax 007HF generator fitted with a rotating chromium anode ( $\lambda = 2.2897$  Å) that was focused on the specimen through a 300- $\mu\text{m}$ -diameter collimator. The instrument's correct sample-to-detector distance was verified by measuring the lattice constant of a LaB<sub>6</sub> standard (NIST 660c). All nanowire samples were prepared using a centrifugation method without salts for precipitation, such as ammonium sulfate, to eliminate background peaks (Fig. 4a,b). Samples were then dialyzed in 150 mM ethanolamine buffer at pH 10.5 and 20  $\mu\text{l}$  solutions containing nanowire samples were dropped from a micropipette onto glass substrates. To ensure data reproducibility, the experiments were repeated at multiple spots that yielded similar results. At least three different surface spots were scanned at a fixed  $1^\circ$  incident angle with no sample rotation in the sample plane. These multiple measurements yielded similar results. To further investigate the pH effect on the stacking, the pH of nanowire sample was changed by applying ethanolamine buffer at pH 7 and pH 2 (Fig. 4a,b). The background was subtracted using smoothing procedure used for XRD data<sup>30</sup> and the data was plotted using IGOR Pro (WaveMetrics, Inc.). Rigaku's 2D Data Processing Software (v.1.0, Rigaku, 2007) was used to integrate the diffraction rings captured by the detector. Peak fitting to determine  $d$ -spacings was carried out using JADE v.9.5.1 (Materials Data, Inc.) with the Pseudo-Voigt peak profile function.

**FTIR.** We used the Agilent Cary 660 FTIR with a Pike Technologies GladiATR single reflection attenuated total reflection geometry with a diamond crystal. All FTIR spectra were collected with spectral resolution of  $4 \text{ cm}^{-1}$ . Final spectra represent an average of 144 individual spectra and are plotted as absorbance versus a background of air. Samples were prepared on a silicon wafer and the reference spectrum of 10 mM KPO<sub>4</sub> was subtracted from the nanowire spectra. An ATR correction and boxcar smoothing were applied using Agilent software (Extended Data Fig. 9a–c). Measurements on air-dried films were compared to samples fully hydrated in D<sub>2</sub>O, which eliminates the strong H<sub>2</sub>O IR absorption in the amide I band; these measurements were found to be equivalent (Extended Data Fig. 9c).

**Raman spectroscopy.** Raman spectroscopy was performed using a 532-nm-green solid-state diode laser (continuous wave, power  $\sim 57$  mW) with a synapse-cooled CCD detector, 600 grating per mm and  $\times 50$  objective (Horiba-Labram HR Evolution). Nanowires prepared in ethanolamine buffer were drop casted on a silicon wafer. Data were collected with an accumulation time of 10 s, averaged over 80 iterations. A minimum of three different locations were measured on each sample. All experiments were repeated on multiple samples that yielded similar results. The instrument was calibrated using the silicon wafer as standard. Data were analyzed with IGOR Pro software (WaveMetrics, Inc.).

**CD spectroscopy.** CD spectra and subsequent analysis with CDPPro were conducted to estimate the secondary-structure fractions of OmcZ and OmcS nanowires. Samples were initially dialyzed in 10 mM of KH<sub>2</sub>PO<sub>4</sub> buffer at pH 7; the protein concentration was determined via the standard bicinchoninic acid assay. CD scans of nanowire samples and buffer background (five replicates) were collected between 190 and 260 nm with a 10- or 2-mm-path-length quartz cuvette using a spectrometer (Chirascan, Applied Photophysics). Using the Pro-Data Chirascan software (Applied Photophysics), all replicate spectra were averaged, the averaged buffer background spectrum was subtracted from all averaged nanowire spectra. The following formula<sup>36</sup> was used to convert raw ellipticity values (millidegrees (mdeg)) (Fig. 6c,d) to molar ellipticity values ( $[\theta]$ ; deg cm<sup>2</sup> dmol<sup>−1</sup>) for secondary structure quantification shown in Supplementary Table 1c:

$$[\theta] = \frac{\text{mdeg} \times \text{MW}}{l \times C}$$

where MW is the mean residue weight,  $l$  is the path length in centimeters and  $C$  is the concentration in mg ml<sup>−1</sup>. Nanowire spectra in molar ellipticity values were entered into the CDPPro software using the CDSSTR method<sup>35</sup>. Solid-state CD experiments were performed similar to solution experiment except the solid sample holder (Chirascan, Applied Photophysics) was used and the film was prepared in manner similar to FTIR experiments.

**Fluorescence microscopy of nanowires.** A 600  $\mu\text{M}$  Thioflavin T (ThT) stock solution was used to bring nanowire solutions to a final concentration of 100  $\mu\text{M}$  ThT. Samples were incubated for 1 h at room temperature before depositing 10  $\mu\text{l}$  of solution on cleaned microscope slides and coverslips. Microscope slides (Fisherfinest Premium catalog no. 12-544-1) and coverslips were sonicated for 20 min each in 1 M KOH, Milli-Q water and finally 70% ethanol before they were air-dried with nitrogen. Control samples that had only ThT or only nanowires did not show any fluorescent fibril structures (Fig. 6e), confirming that the observed fluorescence is due to ThT binding to nanowires. Samples were excited with a 445-nm CW laser (Agilent Technologies MLC 400B) used at 30% of maximum power ( $< 10$  mW). TIRF microscopy images were acquired on an Eclipse TiE microscope (Nikon) equipped with an Andor iXonEM+ DU-897 camera. All images were processed and analyzed using ImageJ software.

**Fluorescence emission spectroscopy of nanowires.** Thioflavin T (ThT) was obtained from Sigma Aldrich; 600  $\mu\text{M}$  stock solutions were prepared by diluting ThT in 10 mM KPO<sub>4</sub> at pH 7, passing the solution through a 0.2- $\mu\text{m}$  filter to remove dye aggregates and verifying the final ThT concentration with ultraviolet–visible light spectroscopy and the ThT extinction coefficient of (36,000 M<sup>−1</sup> cm<sup>−1</sup>) at 412 nm. Nanowire samples were diluted at a 1:1 ratio (v/v) with a solution of 100  $\mu\text{M}$  ThT and incubated at room temperature for 1 h before acquiring spectra with a Fluoromax-4 spectrofluorometer (Horiba Jobin Yvon) in an ultra-micro fluorescence cuvette with an optical path length of 10 mm (PerkinElmer Part No. B0631124). The excitation wavelength was set to 440 nm and emission was recorded at 465–600 nm with 5-nm-excitation and -emission slit widths.

**Modeling of OmcZ.** We modeled the OmcZ monomer using both homology modeling and de novo folding because multiheme cytochromes such as OmcZ have very low sequence identity with other multiheme cytochromes<sup>4</sup>. A BLAST search found only five unique matches to OmcZ, with the top match being the 16-heme cytochrome (PDB 1Z1N) having a sequence identity of 24%. However, this cytochrome had cross-like heme arrangement with only a single parallel-stacked heme pair, whereas the X-ray diffraction studies of OmcZ (Fig. 4a) indicated several parallel pairs. Additionally, we found two proteins with higher sequence identities to OmcZ of 29% (PDB 3ON4) and 36% (PDB 1ZYE), but neither of these contained hemes, making them unusable as templates. The two remaining matches (PDB 6H5L and 4QO5), were both octaheme protein complexes structurally similar to hydroxylamine oxidoreductase (HAO), although they had low sequence identities with OmcZ of 21 and 24%, respectively. From previous CD measurement of purified OmcZ<sup>3</sup>, OmcZ is known to have an unusually high number of beta sheets, around 25%, and contained few alpha helices, only 13%. Comparatively, PDB 4QO5 was only 8% beta sheets and 40% alpha helices, and PDB 6H5L is 2% beta sheets and 66% alpha helices. A search of other similar octaheme proteins in the PDB revealed that they can be divided into two classes: HAO-like proteins and OTR-like (octaheme tetrathionate reductase) proteins. These two classes of octaheme cytochromes had distinct, well-conserved heme arrangements. In addition to alternating parallel and T stacks, HAO-like



proteins have a triple parallel stack between the fourth, sixth and seventh hemes in which two hemes (the fourth and seventh) are coplanar and the remaining sixth heme is stacked atop both. The fourth heme is out of line with the other seven hemes and is often ligated by a small molecule, such as water or  $\text{SO}_2$ , or by amino acids such as lysine. OTR-like cytochromes have a similar overall arrangement but the triple parallel stack is formed earlier in the heme sequence (the second, fourth and fifth hemes), such as in structures with PDB 1SP3 and 4RKM. Therefore, templates for our OmcZ model were chosen based on these two primary heme arrangements (HAO and OTR) and to match the high number of beta sheets found in purified OmcZ<sup>8</sup>. The two templates that best satisfied these criteria were HAO-like PDB 4QO5 and OTR-like PDB 1SP3. Both templates, as well as the other octaheme proteins, had sequences much longer than OmcZ leading to some of the extraneous structure from the templates being excluded from the models, such as the alpha helix cluster in the PDB 4QO5. Alignment with the templates was restricted such that the heme-binding CXXCH sequences matched between both the template and OmcZ to enable the binding of hemes in the model. After the initial structure was built in MODELLER, unbound histidine residues were reoriented to bond to the iron center as the hemes' distal ligands. A unique feature of OmcZ was the three pairs of neighboring histidine residues (H40 and H41, H96 and H97, and H182 and H183) in the protein sequence. Using these histidines as ligands between the T-stacked hemes, protein was found to hold hemes in a rigid conformation and closer than typical T stacks. This could explain the higher heme stacking found in OmcZ (Fig. 4a). Unfolded peptide segments between hemes were refined using the de novo folding procedure in MODELLER.

To fold the long loops in both models, we carried out long timescale classical MD simulations on Anton-2. We first equilibrated each system in a periodic water box for 100 ns using nanoscale molecular dynamics (NAMD) and the CHARMM36 force field. We then performed 2- $\mu\text{s}$  simulations using both the PDB 1SP3- and PDB 4QO5-based models. The 1SP3 model appeared to break between hemes 4 and 5 (a T-stack) and fold in half. The PDB 4QO5 model was more stable even though the distance between parallel stacks (hemes 1/2, 3/5 and 6/7) increased substantially as the protein extended and pulled the hemes apart. Therefore, this model was chosen to build the model of OmcZ.

For final model building, we used the fact that many eight-heme proteins show similar stacking arrangement of hemes<sup>25</sup> as shown in the superposition of heme groups from five HAO-like proteins (Extended Data Fig. 7b, PDB 4QO5, green; PDB 1FGJ, blue; PDB 3GM6, cyan; PDB 6H5L, gray; and PDB 6HIF, pink). The PDB 4QO5 structure was used as the reference for alignment and overlay was performed by minimizing the root mean square distance between the respective hemes' iron centers using the pairwise fitting function within PyMOL. Adding harmonic restraints to the hemes and performing another 2- $\mu\text{s}$  simulation of the 4QO5-based model, we obtained the folding of the protein without the hemes pulling apart. One region appeared to fold into beta sheet-like structures that did not resolve further with longer simulations. MODELLER was used to add formal structure to the regions that seemed to be approaching beta sheets and alpha helices (Extended Data Fig. 7a). We aligned the hemes from each OmcZ model to the low-resolution (20 Å) cryo-EM density map<sup>4</sup>. To refine the fit, we simulated a density map of the hemes with 15 Å resolution using the MDFF plugin in VMD. The highest density in the cryo-EM density map is typically contributed by the hemes<sup>4</sup>. We confirmed this by comparing the alignment of simulated heme density to the high-density components of our 3.7 Å resolution cryo-EM density map of OmcZ. Therefore, the computed density map was compared to the cryo-EM density map filtered to high density (Extended Data Fig. 7c,d).

Building a model for OmcZ was hampered by following challenges. First, a crystal structure is not available. A model could not be determined by cryo-EM. The flexibility of OmcZ and its tendency to form bundles of fibers have severely limited collection of the large number of straight single filaments required for ab initio atomic model building. These challenges have resulted a low-resolution (~20 Å) map that was used for comparison (Fig. 4d).

In the absence of an experimental structure, computational modeling relied on one of two methods to build a model: homology modeling and ab initio folding. The eight hemes bound within OmcZ severely complicate ab initio folding, if not making it entirely impossible using currently available methods. These hemes are not small ligands bound to an active site; they take up a substantial volume at the core of OmcZ and are undoubtedly critical to its structure. Using a sequence homolog as a template for homology modeling is also not feasible. The best amino acid sequence matches were very weak (less than 25% identity), several contained no hemes and most primarily consisted primarily of alpha helices whereas OmcZ contains beta sheets.

However, our OmcZ model does include key features consistent with experiments. First, the family of octaheme c-type cytochrome proteins shares a highly conserved heme arrangement that seems similar to seen at the core of OmcZ using high-contour cryo-EM maps. Second, our model maximizes the number of beta sheets, as indicated by experiments.

The amino acid sequence of OmcZ contains eight hemes with total 17 histidines, including three pairs of adjacent histidine residues distributed across the sequence (H40 and H41, H96 and H97, and H182 and H183). Assuming all hemes in OmcZ are bis-histidine coordinated, a minimum of 16 histidines will be required for axial ligation to eight hemes. Therefore, these adjacent histidine pairs

could be forming a heme ligation that would create a closely held, rigid T-stacked heme pair. This consecutive His-His binding motif found in OmcZ also exists in c3 cytochromes (PDB 1GYO, 2BQ4 and 2E84). However, in OmcZ model, the three pairs of adjacent histidines that bind to T-stacked hemes are all distal histidine ligands. Therefore, they are bound opposite to the proximal histidine in the CXXCH sequence. In contrast, in the c3 cytochromes, all the heme-binding adjacent histidine pairs are mixed, containing both a proximal and a distal histidine. Despite this difference, the distance between the bound hemes remains consistent at ~6 Å (Extended Data Fig. 7e-h). This analysis thus further validates our modeling approach.

**Statistics and reproducibility.** All imaging and measurements were repeated at least over three biological replicates and yielded similar results.

**Reporting Summary.** Further information on research design is available in the Nature Research Reporting Summary linked to this article.

## Data availability

The datasets generated during and/or analyzed during the current study are contained in the published article (and its supplementary information), or available from the corresponding author on reasonable request. Source data are provided with this paper.

## Code availability

The codes used during and/or analyzed during the current study are available from the corresponding author on reasonable request.

## References

- Park, I. & Kim, B.-C. Homologous overexpression of *omcZ*, a gene for an outer surface c-type cytochrome of *Geobacter sulfurreducens* by single-step gene replacement. *Biotechnol. Lett.* **33**, 2043 (2011).
- Vargas, M. et al. Aromatic amino acids required for pili conductivity and long-range extracellular electron transport in *Geobacter sulfurreducens*. *mBio* **4**, e00105–e00113 (2013).
- Wang, F. et al. Cryoelectron microscopy reconstructions of the *Pseudomonas aeruginosa* and *Neisseria gonorrhoeae* type IV pili at sub-nanometer resolution. *Structure* **25**, 1423–1435 (2017).
- Silva, J. C., Gorenstein, M. V., Li, G.-Z., Vissers, J. P. & Geromanos, S. J. Absolute quantification of proteins by LCMSE: a virtue of parallel MS acquisition. *Mol. Cell. Proteom.* **5**, 144–156 (2006).
- Grossmann, J. et al. Implementation and evaluation of relative and absolute quantification in shotgun proteomics with label-free methods. *J. Proteom.* **73**, 1740–1746 (2010).
- Krey, J. F. et al. Accurate label-free protein quantitation with high- and low-resolution mass spectrometers. *J. Proteome Res.* **13**, 1034–1044 (2013).
- Erickson, H. P. Size and shape of protein molecules at the nanometer level determined by sedimentation, gel filtration, and electron microscopy. *Biol. Proced.* **11**, 32 (2009).
- Qin, N. et al. Nanoscale probing of electron-regulated structural transitions in silk proteins by near-field IR imaging and nano-spectroscopy. *Nat. Commun.* **7**, 1–8 (2016).
- Paulite, M. et al. Imaging secondary structure of individual amyloid fibrils of a  $\beta$ 2-microglobulin fragment using near-field infrared spectroscopy. *J. Am. Chem. Soc.* **133**, 7376–7383 (2011).
- Ramer, G., Ruggeri, F. S., Levin, A., Knowles, T. P. & Centrone, A. Determination of polypeptide conformation with nanoscale resolution in water. *ACS Nano* **12**, 6612–6619 (2018).
- Ruggeri, F. et al. Infrared nanospectroscopy characterization of oligomeric and fibrillar aggregates during amyloid formation. *Nat. Commun.* **6**, 1–9 (2015).
- Ruggeri, F. et al. Nanoscale studies link amyloid maturity with polyglutamine diseases onset. *Sci. Rep.* **6**, 1–11 (2016).
- Kocun, M., Labuda, A., Meinhold, W., Revenko, I. & Proksch, R. Fast, high resolution, and wide modulus range nanomechanical mapping with bimodal tapping mode. *ACS Nano* **11**, 10097–10105 (2017).
- Bruckner, S. Estimation of the background in powder diffraction patterns through a robust smoothing procedure. *J. Appl. Crystallogr.* **33**, 977–979 (2000).

## Acknowledgements

We thank D. Lovley (University of Massachusetts, Amherst) and K. Inoue (University of Miyazaki) for providing strains and OmcZ antibody as well as E. Yan, E. Martz, F. Samatey, C. Salgueiro, C. Shippis and Y. Xiong for helpful discussions. We also thank C. Leang for providing the protocol for immunogold labeling, T. Gokus from Neaspec for help with nanoscale IR imaging and M. Shahid Mansuri, J. Kanyo and T. Lam for help with mass-spectrometry analysis. A portion of the research was performed using Environmental Molecular Sciences Laboratory (EMSL, Ringgold ID 130367), a Department of Energy (DOE) Office of Science User Facility sponsored by the Office

of Biological and Environmental Research. S.E.Y. thanks M. Raschke, J. Atkin and S. Lea for help with building the IR *s*-SNOM setup and C. Smallwood for help with bacteriorhodopsin sample preparation. We thank T. Walsh from Asylum Research for help with stiffness measurements. At Yale, we thank W. Gray from C. Jacobs-Wagner's laboratory for help with fluorescence microscopy and Z. Wu from H. Wang's laboratory for help with Raman studies. Computational work was supported by the Air Force Office of Scientific Research Grant FA9550-17-0198 (V.S.B.) and high-performance computing time from the National Energy Research Scientific Computing Center and from the high-performance computing facilities at Yale as well as supercomputer time from the Extreme Science and Engineering Discovery Environment under grant no. TG-CHE170024 (A.A.). Anton 2 computer time was provided by the Pittsburgh Supercomputing Center (PSC) through Grant R01GM116961 from the National Institutes of Health (NIH). The Anton 2 machine at PSC was generously made available by D.E. Shaw Research. This research was supported by the Career Award at the Scientific Interfaces from Burroughs Wellcome Fund (N.S.M.), the NIH Director's New Innovator award no. 1DP2AI138259-01 (N.S.M.), the National Science Foundation (NSF) CAREER award no. 1749662 (N.S.M.). Research was sponsored by the Defense Advanced Research Project Agency Army Research Office and was accomplished under Cooperative Agreement Number W911NF-18-2-0100 (N.S.M. and V.S.B.). This research was supported by NSF Graduate Research Fellowship awards 2017224445 (J.P.O.). Research in the laboratory is also supported by the Charles H. Hood Foundation Child Health Research Award (N.S.M.) and The Hartwell Foundation Individual Biomedical Research Award (N.S.M.).

### Author contributions

S.E.Y. and N.S.M. conceived and designed the study. S.E.Y. built the quantum cascade laser-coupled IR *s*-SNOM detection interferometer, prepared samples, performed AFM, IR *s*-SNOM measurements, imaged immunogold-labeled nanowires

with AFM along with imaging and analysis of reduction in nanowire diameter. J.P.O. grew biofilms in microbial fuel cell and analyzed protein content with R.J. K.R. built the OmcZ model and performed simulations, with help from P.J.D., under the guidance of V.S.B. J.P.O. and W.H. purified nanowires from bacteria, performed CD experiments and conducted analysis. J.P.O. performed FTIR and fluorescence emission spectroscopy and analyzed data with S.E.Y. W.H. and S.E.Y. performed principal component analysis on the IR *s*-SNOM data. V.S. and Y.G. imaged immunogold-labeled nanowires with TEM. Y.G. also carried out CP-AFM measurements and analyzed data with P.J.D. Y.G. and S.E.Y. performed and analyzed nanowire stiffness measurements. S.M.Y. carried out mass spectroscopy as well as Raman spectroscopy and analyzed Raman data with S.E.Y. Electrode fabrication using electron-beam lithography was carried out by D.V. and Y.G. S.E.Y. and T.V. performed XRD measurements and analyzed data with Y.G. A.A. and S.C. performed initial molecular dynamics simulations under the guidance of V.S.B. A.A. constructed the models, coded the analysis scripts and performed the analysis of molecular dynamics data. N.S.M. supervised the project. S.E.Y. and N.S.M. cowrote the manuscript with input from all authors.

### Competing interests

The authors declare no competing interests.

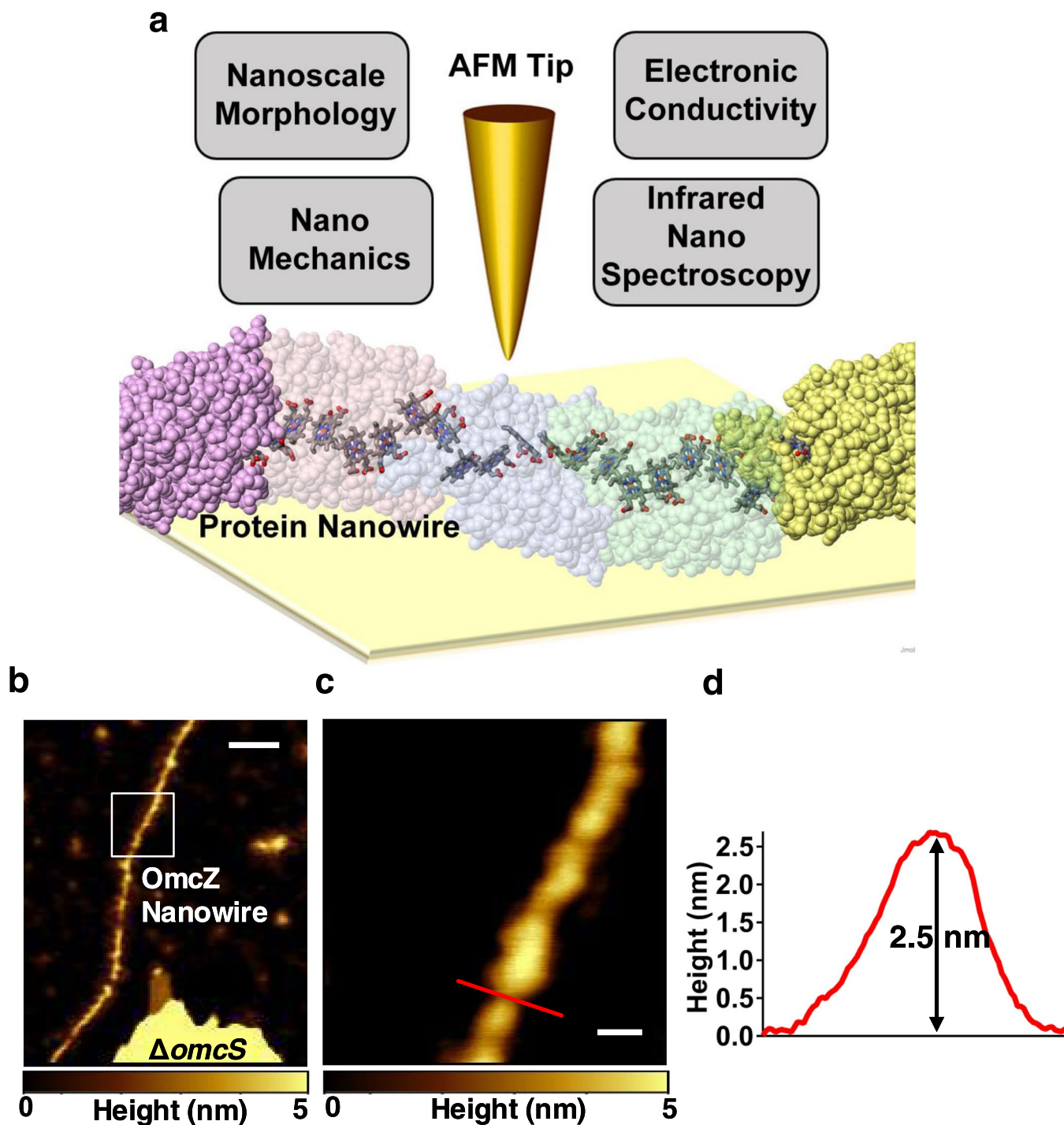
### Additional information

**Extended data** is available for this paper at <https://doi.org/10.1038/s41589-020-0623-9>.

**Supplementary information** is available for this paper at <https://doi.org/10.1038/s41589-020-0623-9>.

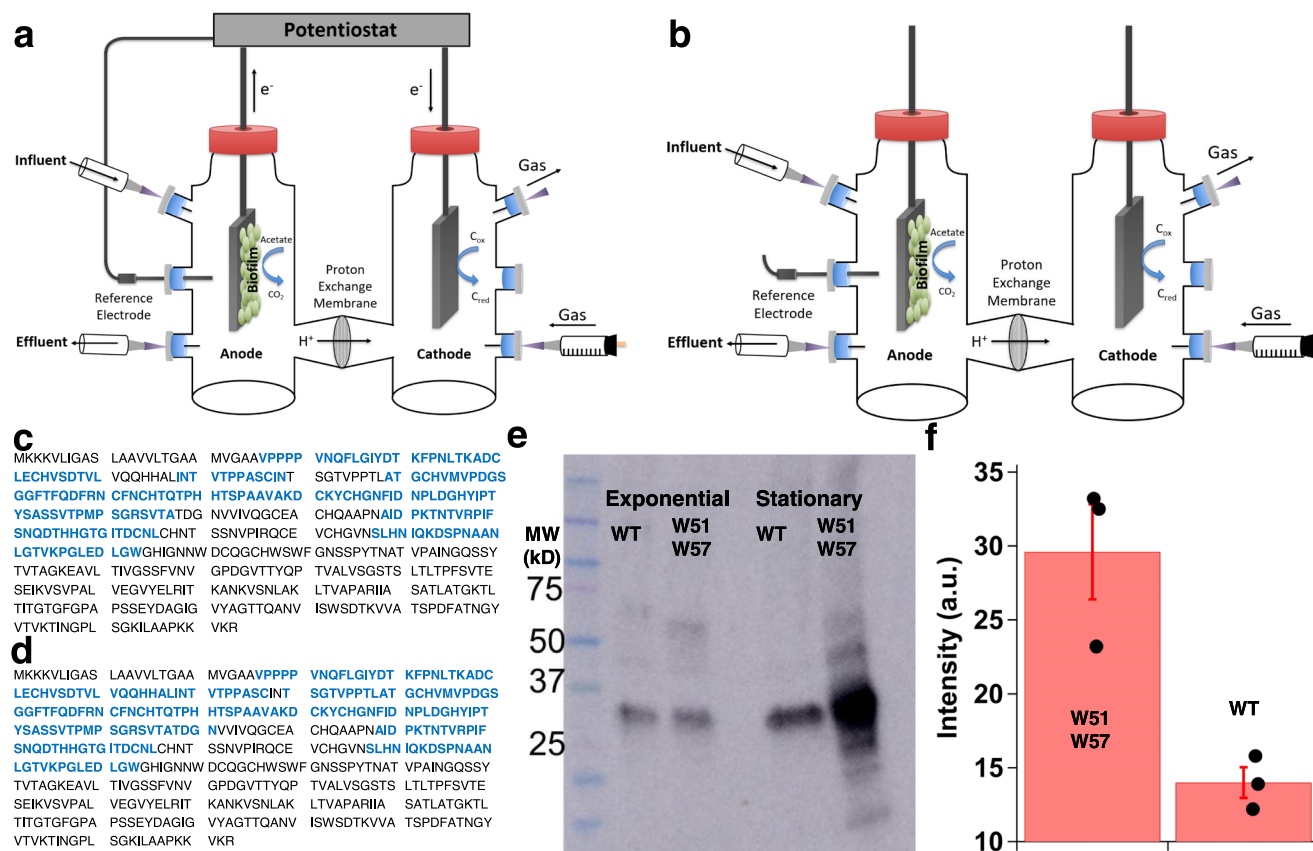
**Correspondence and requests for materials** should be addressed to S.E.Y. or N.S.M.

**Reprints and permissions information** is available at [www.nature.com/reprints](http://www.nature.com/reprints).

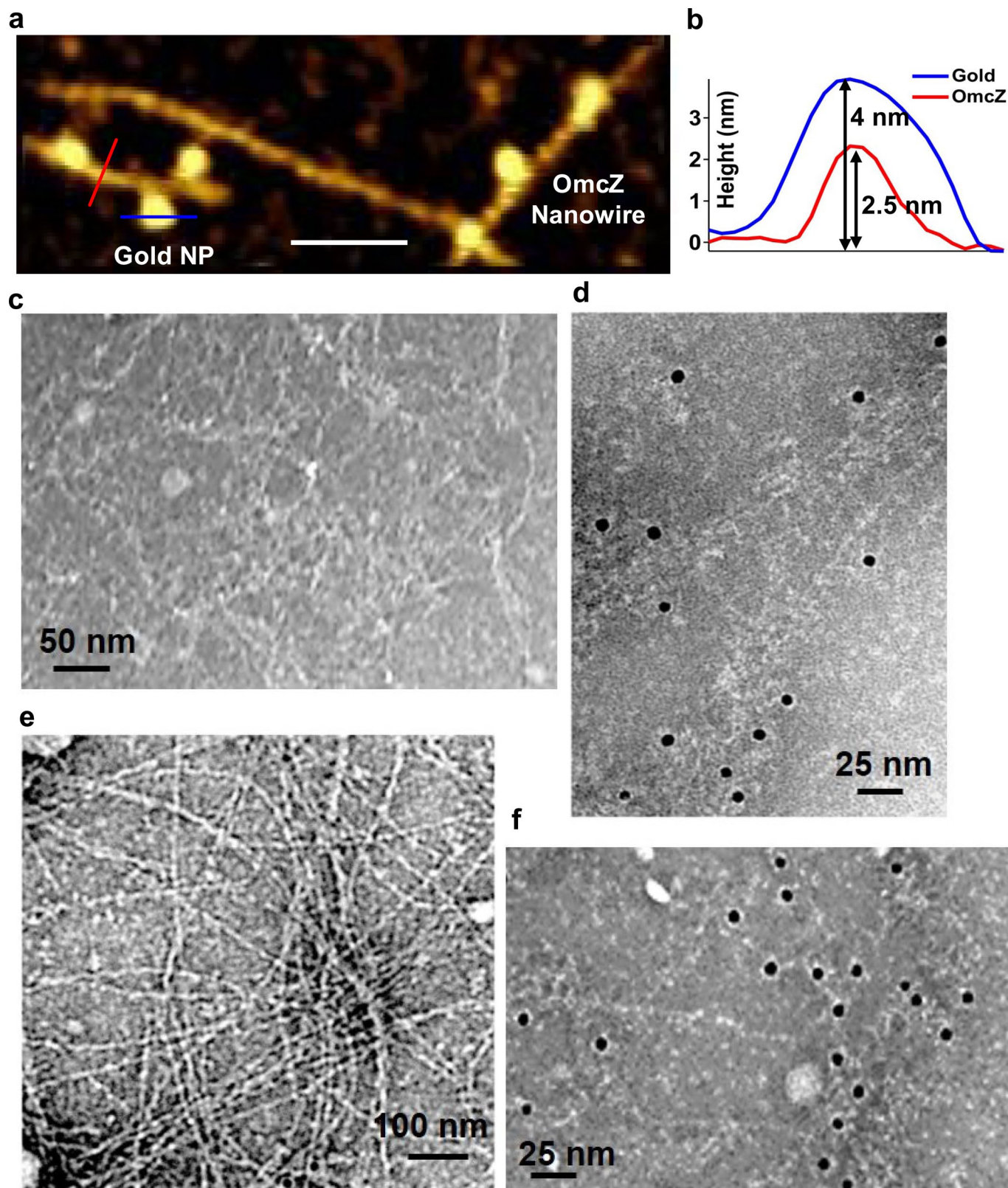


**Extended Data Fig. 1 | Multimodal imaging and nanospectroscopy platform to determine the structure of individual OmcZ and OmcS nanowires as well as their electrical and mechanical properties. a**, Multimodal platform with OmcS nanowire structure showing stacked hemes providing electron transport path (PDB ID: 6EF8). **b, c**, OmcZ nanowires produced by  $\Delta omcS$  strain grown under conditions that overexpress OmcZ. **b**, AFM images of OmcZ nanowires of  $\Delta omcS$  strain. **c**, Zoomed image of OmcZ nanowire shown in white square in **b**. **d**, AFM Height profile of the OmcZ nanowire taken at the a location shown by a red line in **c**. Scale bars: **b**, 100 nm **c**, 20 nm.

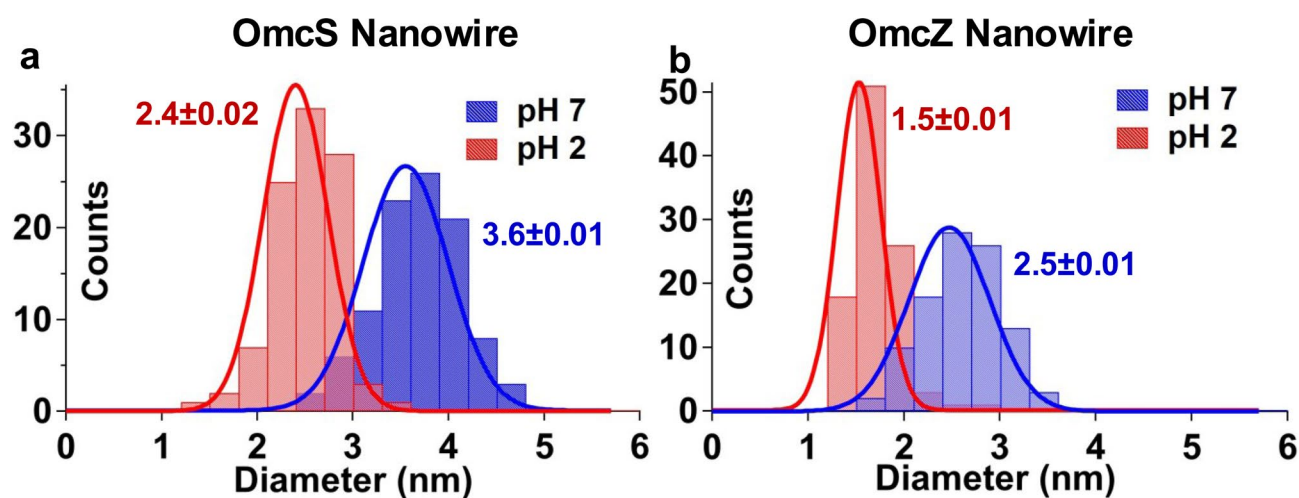




**Extended Data Fig. 2 | Mass spectrometry and immunoblotting of filament preparations confirm electric field induces overexpression of OmcZ in biofilms.** **a, b**, Strategy to evaluate the effect of an electric field on the production of OmcZ nanowires. Wild-type *G. sulfurreducens* cells were grown with a continuous supply of fumarate on graphite electrodes as anodes in a microbial fuel cell. **a**, An electric field was supplied during the growth of current-producing biofilms by connecting anode to cathode via a potentiostat. **b**, The electric-field was absent after disconnecting the anodes from the cathodes. OmcZ peptide coverage (blue) in filament preparations of **c**, Wild-type (WT) and **d**, W51W57 strain confirming the presence of an extracellular (30 kDa) form of OmcZ that forms nanowires. Comparison of OmcZ abundance in filament preparations of WT and W51W57 strains using **e**, Immunoblotting and **f**, Mass spectrometry showing higher level of OmcZ in W51W57 strain than WT. Data represent mean  $\pm$  standard deviation ( $n=3$  biologically independent samples overlaid as black circles).

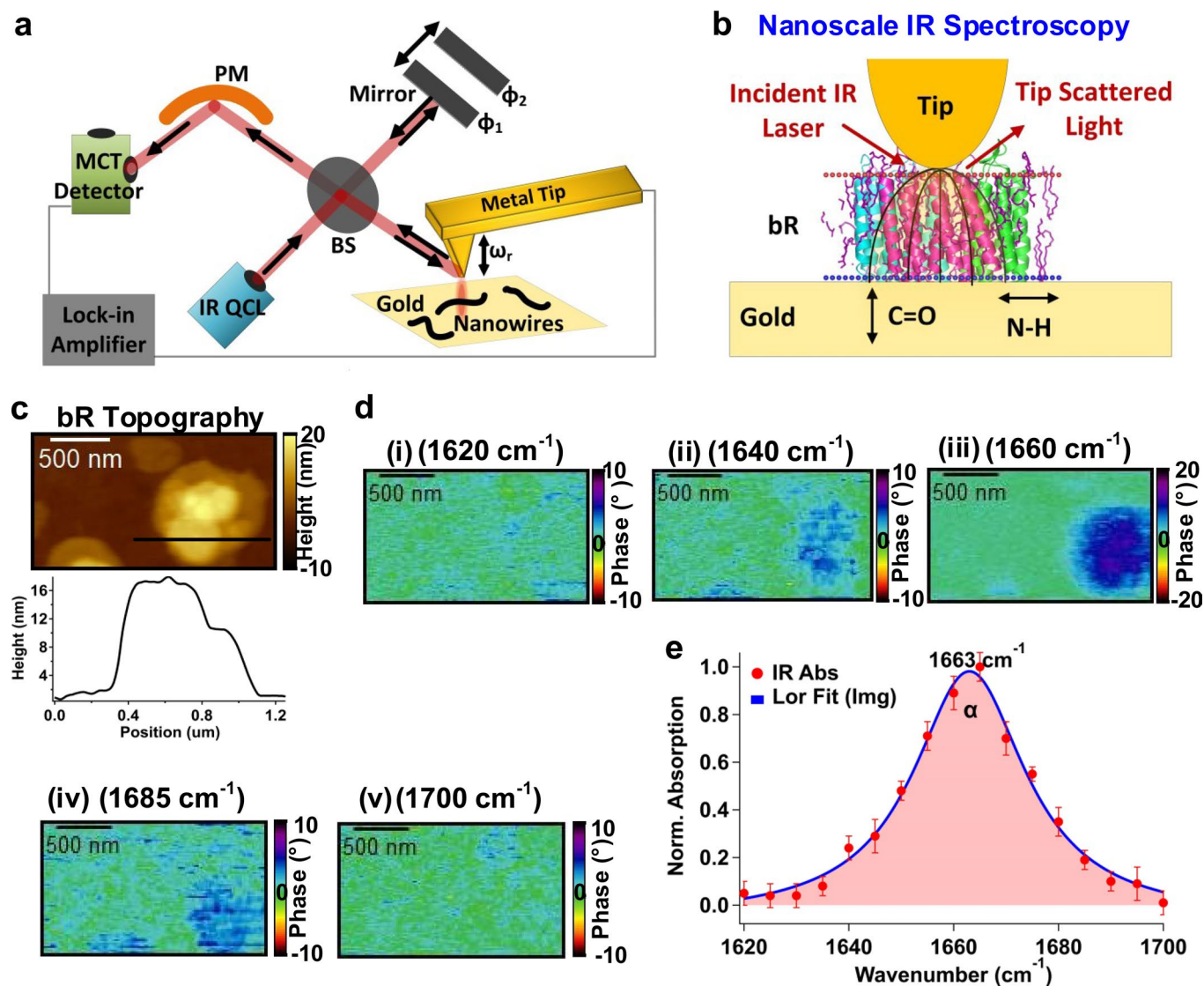


**Extended Data Fig. 3 | Immunogold labeling confirms the identity of OmcZ nanowires.** **a**, AFM image of immunogold-labelled OmcZ nanowire. **b**, heights of nanowire (red) and gold nanoparticle (blue) at locations shown in **a**. **c-f**, TEM images of OmcZ nanowires of ZKI strain in the **c**, absence of OmcZ antibody and **d**, in the presence of anti-OmcZ antibody. Secondary antibody with gold nanoparticles was used in both **c-e**. No OmcZ labelling was found for filaments of  $\Delta omcZ$  strain **f**, Labelling for OmcZ nanowires of W51W57 strain. Scale bars, **a**, 100 nm, **c**, 50 nm, **d**, 25 nm, **e**, 100 nm, **f**, 25 nm.

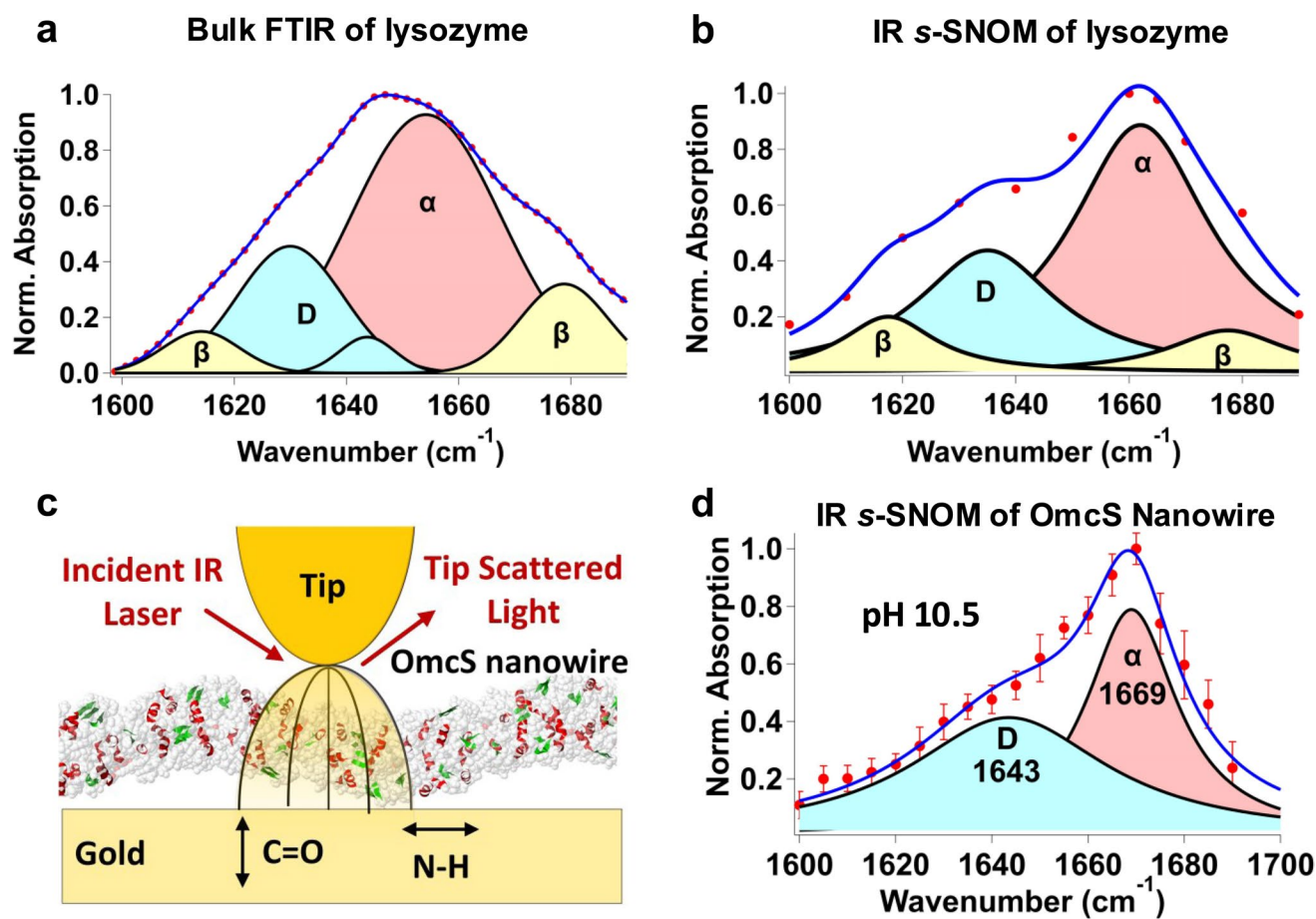


**Extended Data Fig. 4 | Low pH reduces the diameter of individual OmcS and OmcZ nanowires.** Histograms of AFM measurements of OmcS and OmcZ nanowire heights showed that lowering the pH reduced the diameter of **a**, OmcS and **b**, OmcZ nanowires. Values represent mean  $\pm$  standard deviation (s.d.) ( $n=100$  measurements of nanowires over 3 biologically independent samples).

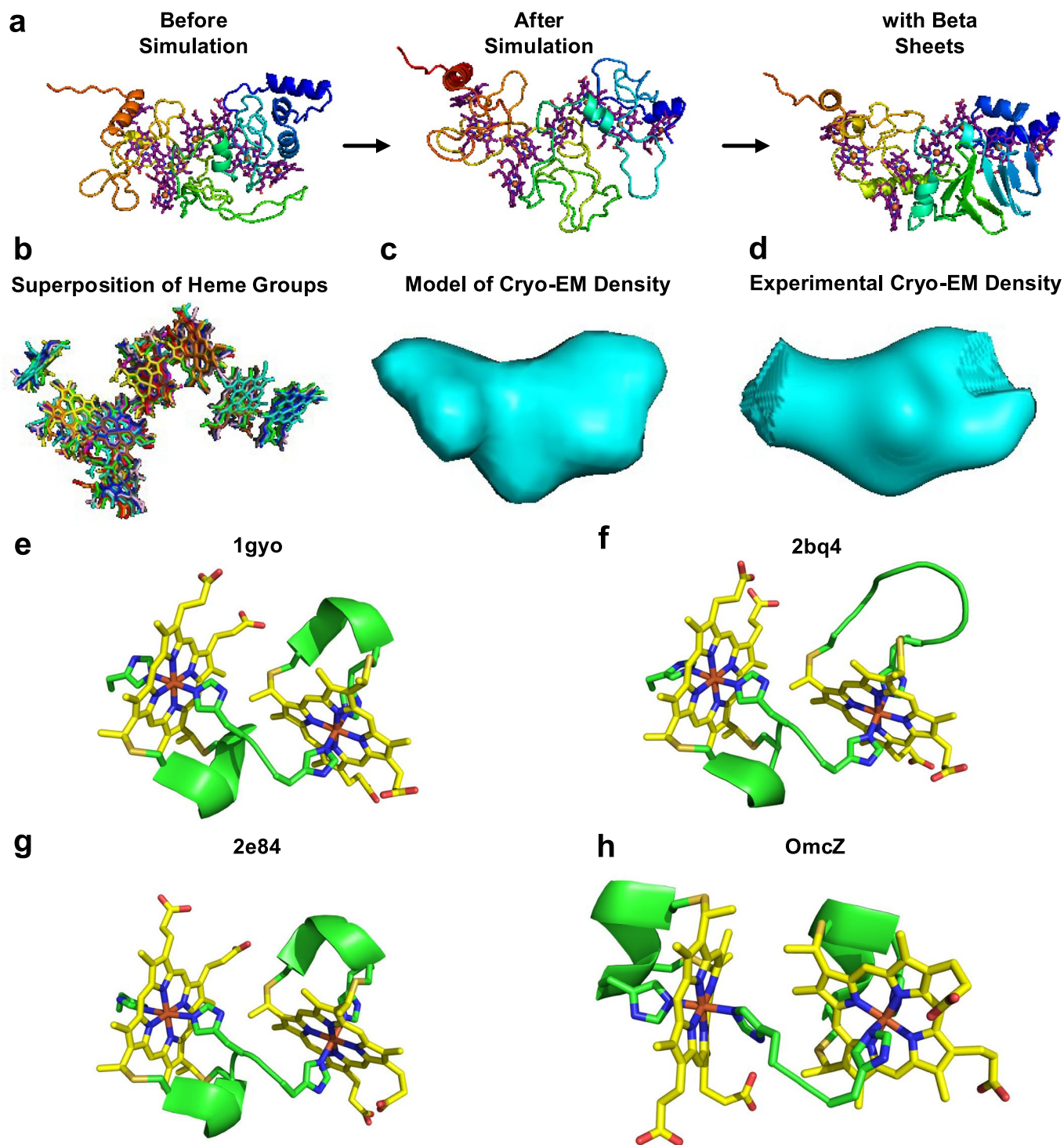




**Extended Data Fig. 5 | IR s-SNOM imaging of bacteriorhodopsin (bR) confirms  $\alpha$ -helical structure.** **a, b** Schematic of IR s-SNOM. **a**, The interferometer is comprised of a tunable quantum cascade laser (QCL) for tip illumination, a beam splitter (BS), a detector (Mercury Cadmium Telluride, MCT), a parabolic mirror (PM), and a reference mirror. **b**, Schematic of the IR s-SNOM setup used for bR imaging (PDB ID: 1m0I). All helices are parallel to electric field lines that enhance the amide I signal. **c**, AFM topography and corresponding height profile for bR taken at a location shown by a black line. **d**, IR s-SNOM near-field phase (absorption) images for bR at various IR excitations. At 1660  $\text{cm}^{-1}$  (iii, on-resonant IR), the amide I absorption is enhanced in the near-field phase data. However, when changed to other frequencies (i–ii & iv–v, off-resonance), the phase signal decreases and drops to zero. **e**, Spatiospectral analysis of near-field phase data for the amide I mode of bacteriorhodopsin. The blue line corresponds to a fit of the imaginary part of a Lorentzian (Lor) with peak at 1663  $\text{cm}^{-1}$  and line width of 25  $\text{cm}^{-1}$ . Data represent mean  $\pm$  standard deviation for individual bR proteins ( $n=3$  biologically independent samples).



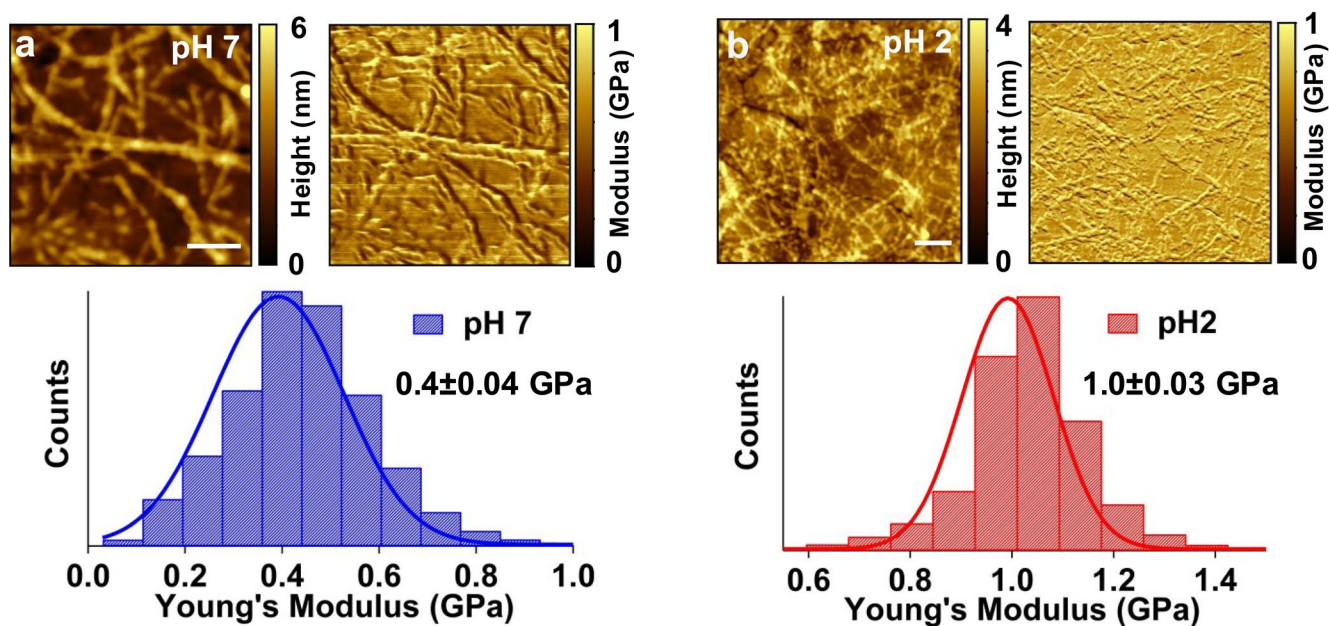
**Extended Data Fig. 6 | Bulk FTIR and IR s-SNOM confirm lysozyme structure and IR s-SNOM spectroscopy of OmcS nanowires agrees with Cryo-EM structure.** Multi-peak fitting function was used to fit the data using **a**, Gaussian profile for bulk FTIR and **b**, a Lorentzian profile for IR s-SNOM data.  $\alpha$ -helix corresponds to 1662  $\text{cm}^{-1}$ ,  $\beta$ -sheet corresponds to 1618  $\text{cm}^{-1}$  and 1678  $\text{cm}^{-1}$ , and the loop (D) region corresponds to 1635  $\text{cm}^{-1}$ . **c**, Schematic of the IR s-SNOM setup for nanowire imaging. Secondary structure of the OmcS nanowire at pH 10.5 is shown in **a** (PDB ID: 6EF8) with  $\alpha$ -helices in red,  $3_{10}$  helices in pink and beta strands in green. **d**, At pH 10.5 used to solve the structure of OmcS nanowires, spatio-spectral analysis of near-field phase data of the amide I mode of OmcS nanowire. The blue line corresponds to a fit of imaginary parts of a Lorentzian, with peak positions at 1669  $\text{cm}^{-1}$  and 1643  $\text{cm}^{-1}$  corresponding to  $\alpha$ -helical and loop regions respectively. Data represent mean  $\pm$  standard deviation for individual OmcS nanowires ( $n=3$  biologically independent samples).



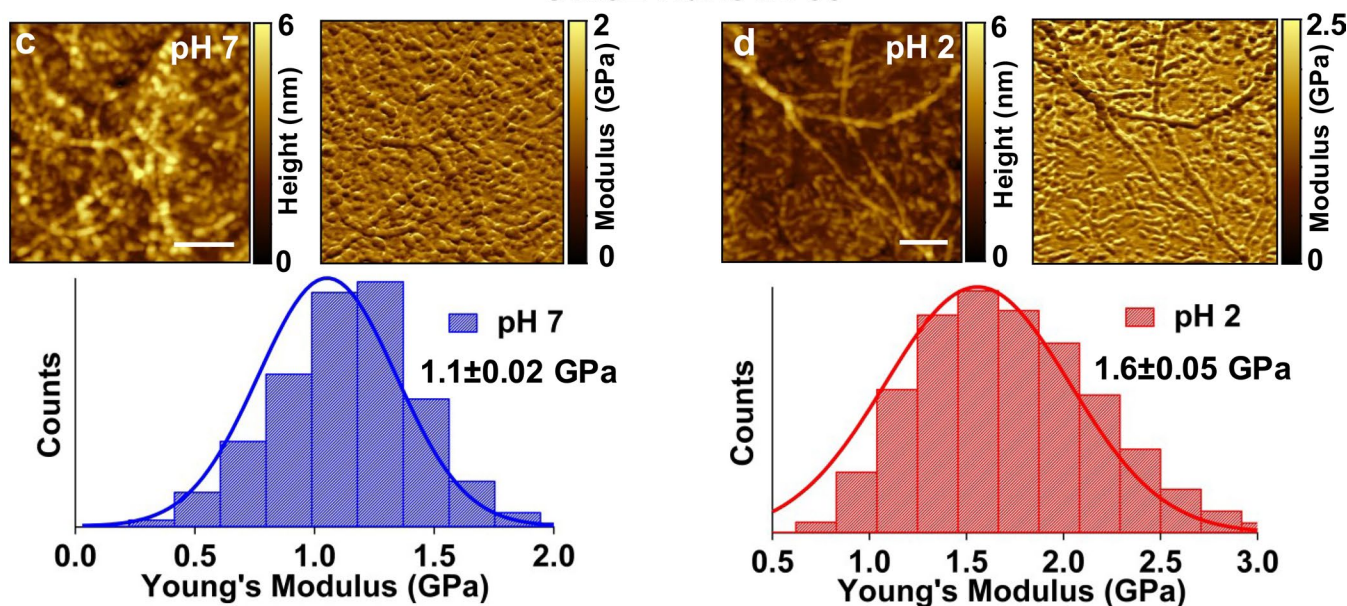
**Extended Data Fig. 7 | Model of OmcZ structure reveals highly stacked hemes and beta sheets in agreement with experiments.** **a**, Computational model of OmcZ. **b**, Superposition of hemes from five 8-heme cytochromes (PDB ID:4QO5:Green, 1FGJ:Blue, 3GM6:Cyan, 6H5L:Gray, and 6HIF:Pink). Both **c**, computed and **d**, experimental cryo-EM density for OmcZ show similar shape and size. **e-h**, Consecutive histidines cause tight heme T-junction. The His-His binding motif found in OmcZ also exists in c3 cytochromes, (PDB ID: **e**, 1gyo, **f**, 2bq4, and **g**, 2e84). In OmcZ model (**h**), the three pairs of adjacent histidines that bind to T-stacked hemes are all distal histidine ligands bound opposite to the proximal histidine in the CXXCH sequence. In the c3 cytochromes, all the heme-binding adjacent histidine pairs are mixed, containing both a proximal and a distal histidine. Despite this difference, the distance between the heme pairs for c3 and OmcZ is similar (~6.0 Å).



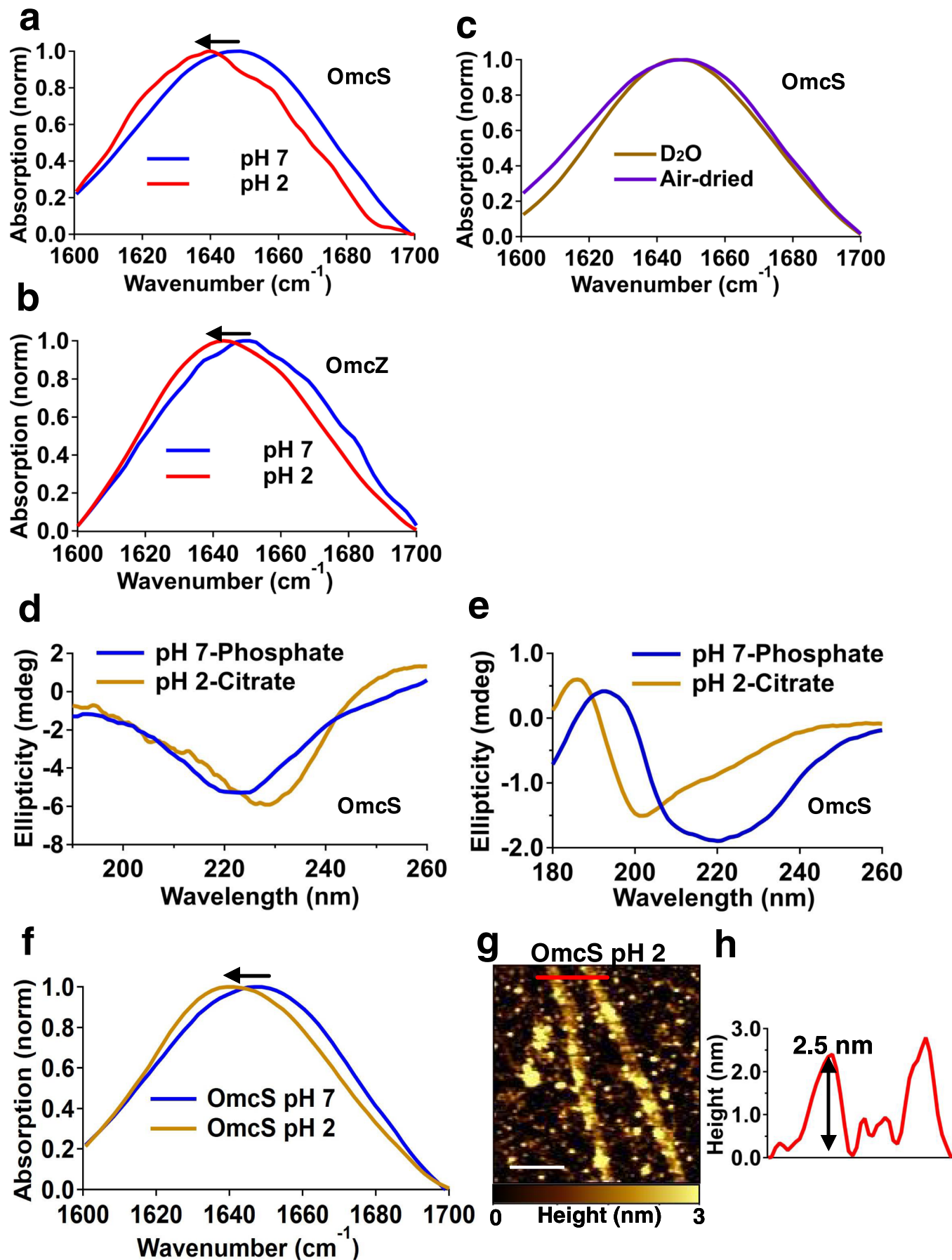
## OmcS Nanowires



## OmcZ Nanowires



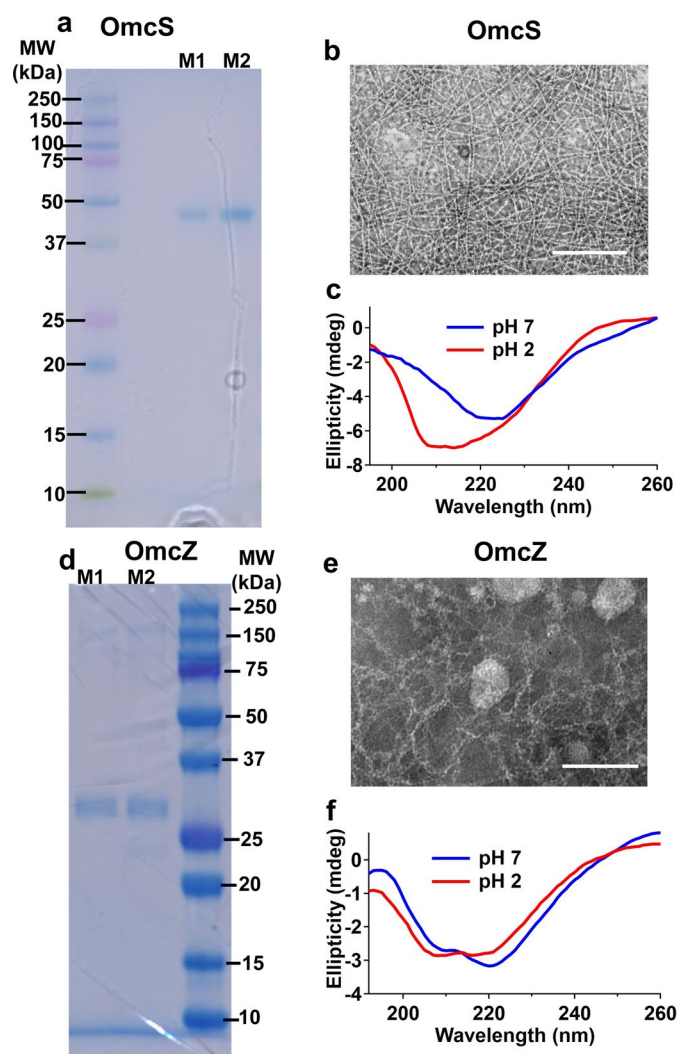
**Extended Data Fig. 8 | Reduction in nanowire diameter enhances their stiffness.** AFM topography, Young's modulus, and the stiffness distribution for OmcS nanowires at **a**, pH 7 and **b**, pH 2 and for OmcZ nanowires **c**, pH 7 and **d**, pH 2. Scale bars: **a** and **d**, 100 nm; **b** and **c**, 200 nm. Values represent mean  $\pm$  (s. d.) for  $n = 512 \times 512$  measurements of nanowires over three biologically independent samples.



Extended Data Fig. 9 | See next page for caption.

**Extended Data Fig. 9 | Bulk FTIR spectra of OmcS and OmcZ nanowires show transition to  $\beta$ -sheets at pH 2 and conformation change is independent of buffers.** FTIR spectra at pH 7 and pH 2 for **a**, OmcS nanowires and **b**, OmcZ nanowires showing a red shift, consistent with transition to  $\beta$ -sheets. **c**, Water does not contribute to the amide I spectra because OmcS nanowires at pH 7 under air-dried and D<sub>2</sub>O conditions display similar spectra. **d**, **e**, OmcS nanowires at pH 7 and pH 2 in 10 mM Potassium Phosphate and 20 mM Citrate buffer characterized by **d**, Solution CD spectra and **e**, Solid-state CD spectra. **f**, FTIR spectra for OmcS nanowires in Citrate buffer at pH 2 showing a red shift, consistent with transition to  $\beta$ -sheets. **g**, Representative AFM image and **h**, corresponding height profile at a location shown by a red line in **g** for OmcS nanowires in citrate buffer at pH 2 under air-dried conditions. Scale bar, 200 nm.





**Extended Data Fig. 10 | Purified OmcS and OmcZ nanowires from  $\Delta omcZ$  and KN400 strains respectively show conformational change to  $\beta$ -sheets similar to nanowires of wild-type and W51W57 strains.** SDS-PAGE gel of filament preparations showing a single band corresponding to **a**, OmcS purified from  $\Delta omcZ$  strain and **c**, OmcZ from KN400 strain. Corresponding TEM images of **b**, OmcS and **e**, OmcZ nanowires. Scale bars, 400 nm. Solution CD spectra of **c**, OmcS and **f**, OmcZ is similar to CD spectra of OmcS and OmcZ nanowires purified from wild-type and W51W57 strains respectively (Fig. 6c, d). M1 and M2 represent nanowires sheared from cells by two different methods – vortexing (M1) and blending (M2).

## Reporting Summary

Nature Research wishes to improve the reproducibility of the work that we publish. This form provides structure for consistency and transparency in reporting. For further information on Nature Research policies, see [Authors & Referees](#) and the [Editorial Policy Checklist](#).

### Statistics

For all statistical analyses, confirm that the following items are present in the figure legend, table legend, main text, or Methods section.

- |                                     |  |
|-------------------------------------|--|
| n/a                                 | Confirmed  |
| <input type="checkbox"/>            | <input checked="" type="checkbox"/> The exact sample size ( $n$ ) for each experimental group/condition, given as a discrete number and unit of measurement  |
| <input type="checkbox"/>            | <input checked="" type="checkbox"/> A statement on whether measurements were taken from distinct samples or whether the same sample was measured repeatedly  |
| <input checked="" type="checkbox"/> | <input type="checkbox"/> The statistical test(s) used AND whether they are one- or two-sided<br><i>Only common tests should be described solely by name; describe more complex techniques in the Methods section.</i>  |
| <input checked="" type="checkbox"/> | <input type="checkbox"/> A description of all covariates tested  |
| <input checked="" type="checkbox"/> | <input type="checkbox"/> A description of any assumptions or corrections, such as tests of normality and adjustment for multiple comparisons   |
| <input type="checkbox"/>            | <input checked="" type="checkbox"/> A full description of the statistical parameters including central tendency (e.g. means) or other basic estimates (e.g. regression coefficient) AND variation (e.g. standard deviation) or associated estimates of uncertainty (e.g. confidence intervals) |
| <input checked="" type="checkbox"/> | <input type="checkbox"/> For null hypothesis testing, the test statistic (e.g. $F$ , $t$ , $r$ ) with confidence intervals, effect sizes, degrees of freedom and $P$ value noted<br><i>Give <math>P</math> values as exact values whenever suitable.</i>                                       |
| <input checked="" type="checkbox"/> | <input type="checkbox"/> For Bayesian analysis, information on the choice of priors and Markov chain Monte Carlo settings  |
| <input checked="" type="checkbox"/> | <input type="checkbox"/> For hierarchical and complex designs, identification of the appropriate level for tests and full reporting of outcomes  |
| <input checked="" type="checkbox"/> | <input type="checkbox"/> Estimates of effect sizes (e.g. Cohen's $d$ , Pearson's $r$ ), indicating how they were calculated  |

*Our web collection on [statistics for biologists](#) contains articles on many of the points above.*

### Software and code

Policy information about [availability of computer code](#)

Data collection: No special software code was used to collect data

Data analysis: Following softwares were used to analyze data; Asylum Research v.16, IGOR Pro v.7, Gwyddion v. 2.55, ImageJ 1.53c, BLAST 2.10.1

For manuscripts utilizing custom algorithms or software that are central to the research but not yet described in published literature, software must be made available to editors/reviewers. We strongly encourage code deposition in a community repository (e.g. GitHub). See the Nature Research [guidelines for submitting code & software](#) for further information.

### Data

Policy information about [availability of data](#)

All manuscripts must include a [data availability statement](#). This statement should provide the following information, where applicable:

- Accession codes, unique identifiers, or web links for publicly available datasets
- A list of figures that have associated raw data
- A description of any restrictions on data availability

The datasets generated during the current study are available from the corresponding author on reasonable request. Datasets used in this study: PDB 1Z1N, 3ON4, 1ZYE, 4QO5, 1FGJ, 3GM6, 6HIF, 6H5L, 1GYO, 2BQ4, and 2E84

# Field-specific reporting

Please select the one below that is the best fit for your research. If you are not sure, read the appropriate sections before making your selection.

☒ Life sciences ☐ Behavioural & social sciences ☐ Ecological, evolutionary & environmental sciences

For a reference copy of the document with all sections, see [nature.com/documents/nr-reporting-summary-flat.pdf](https://www.nature.com/documents/nr-reporting-summary-flat.pdf)

## Life sciences study design

All studies must disclose on these points even when the disclosure is negative.

Sample size	Sample sizes were based upon accepted conventions within the field ( 3 biological replicates) and no explicit power analysis were carried out.
Data exclusions	No data were excluded from analysis.
Replication	All experiments were independently repeated at least three times and all attempts to replicate the experiments were successful.
Randomization	Randomization was not relevant to the study as all samples were treated similarly either for nanoscale or bulk studies.
Blinding	Investigators were not blinded to group allocation during data collection or analysis as all samples were treated similarly either for nanoscale or bulk studies.

## Reporting for specific materials, systems and methods

We require information from authors about some types of materials, experimental systems and methods used in many studies. Here, indicate whether each material, system or method listed is relevant to your study. If you are not sure if a list item applies to your research, read the appropriate section before selecting a response.

### Materials & experimental systems

n/a	Involved in the study
<input type="checkbox"/>	<input checked="" type="checkbox"/> Antibodies
<input checked="" type="checkbox"/>	<input type="checkbox"/> Eukaryotic cell lines
<input checked="" type="checkbox"/>	<input type="checkbox"/> Palaeontology
<input checked="" type="checkbox"/>	<input type="checkbox"/> Animals and other organisms
<input checked="" type="checkbox"/>	<input type="checkbox"/> Human research participants
<input checked="" type="checkbox"/>	<input type="checkbox"/> Clinical data

### Methods

n/a	Involved in the study
<input checked="" type="checkbox"/>	<input type="checkbox"/> ChIP-seq
<input checked="" type="checkbox"/>	<input type="checkbox"/> Flow cytometry
<input checked="" type="checkbox"/>	<input type="checkbox"/> MRI-based neuroimaging

## Antibodies

Antibodies used	Custom polyclonal anti-OmcZ antibody was synthesized by LifeTein (New Jersey) by immunizing two rabbits with synthetic peptide sequence (DSPNAANLGTVPGL) containing targeted epitope on the native protein, OmcZ, and then affinity purifying the serum against that peptide sequence. Secondary antibodies used : Cat. No. 111-205-144: 12 nm Colloidal Gold AffiniPure Goat Anti-Rabbit IgG (H+L) (EM Grade, Jackson ImmunoResearch Laboratories, Inc.) and Cat. No. 111-195-144: 6 nm Colloidal Gold AffiniPure Goat Anti-Rabbit IgG (H+L) (EM Grade, Jackson ImmunoResearch Laboratories, Inc.).
Validation	The antibody was verified using OmcZ knock out strain and has been independently verified previously (Ref. 8,10)